separation (solvent system, acetonitrile–water; column, Imtakt Unison UK-C18C (Kyoto, Japan), 4.6 mm ID × 250 mm; flow rate, 2.0 mL/min; detection, UV 254 nm) to give 12 fractions (Fr.7–1 to 7–12) and glycyrin (2.5 mg; Fr.7–9). Fr.7–6 was purified by recycling HPLC (Condition A) to afford glycycoumarin (0.7 mg). Fr.8- to Fr.10 were combined and then re-chromatographed by HPLC (solvent system, acetonitrile–water; column, Imtakt Unison UK-C18C, 4.6 mm ID × 250 mm; flow rate, 2.0 mL/min; detection, UV 254 nm) to give 15 fractions (Fr.8–1 to Fr.8–15). Fr.8–3 was subjected to recycling HPLC (Condition A) to give liquiritigenin (1.2 mg). Fr.8–9 was purified by recycling HPLC (Condition A) to afford glycyrol (1.1 mg). The ^{1}H- and ^{13}C-NMR spectra were measured with a Jeol ECA 500 spectrometer (500 MHz; Tokyo, Japan). HPLC was performed on a JASCOLC-2000 plus system (Tokyo, Japan).

Chemicals

Glycyrrhizic acid (cat. no. 074-03481), glycyrrhizic acid mono-ammonium salt *n*-hydrate (cat. no. 075-02171), glycyrrhetinic acid (cat. no. 072-02181) and glabridin (cat. no. 070-04821) were purchased from Wako Pure Chemical Industries (Osaka, Japan). Liquiritin (cat. no. L8045), liquiritigenin (cat. no. 78825) and licochalcone A (cat. no. 68783) were purchased from Sigma–Aldrich (Tokyo, Japan) and isoliquiritigenin (cat. no. I0822) from Tokyo Chemical Industry (Tokyo, Japan). Licorice-saponins G2 (cat. no. P2502) and H2 (cat. no. P2503), and glycyrrhetic acid 3-*O*-glucuronide (cat. no. NH080502) were purchased from Funakoshi (Tokyo, Japan). Glycycoumarin, glycyrol, glycyrin and liquiritigenin were isolated from *G. uralensis* extracts in this study, as described above.

Analysis of anti-HCV activity of plant extracts and purified compounds

Test samples were weighed and dissolved in DMSO to obtain stock solutions at 10 or 30 mg/mL. The stock solutions were stored at −20 °C until used. Huh7.5 cells were seeded in 24-well plates (1.6×10^5 cells/well). HCV was mixed with serial dilutions of the test samples (100, 30, 10, 3 and 1 μg/mL) and inoculated into the cells. After 2 hr, the cells were washed with medium to remove residual virus and further incubated in medium containing the same concentrations of the samples as those during virus inoculation. In time-of-addition experiments, treatment with the samples was performed only during or after virus inoculation in order to assess the mode of action of the samples examined. Culture supernatants were collected 1 and 2 days post-infection and titrated for virus infectivity, as described below. Virus and cells treated with medium containing 0.1% DMSO served as controls. Percent inhibition of the virus infectivity for each dilution of the samples was calculated by comparison with mock-treated controls and IC_{50} determined.

Virus titration

Virus samples were diluted serially 10-fold in complete medium and inoculated onto Huh7.5 cells seeded on glass coverslips in a 24-well plate. After virus adsorption for 2 hr, the cells were washed with medium to remove residual virus and cultured for 24 hr. The virus-infected cells were stained with an indirect immunofluorescence method as reported previously (27). In brief, the virus-infected cells were washed with PBS, fixed with 4% paraformaldehyde for 15 min and permeabilized with 0.1% Triton X-100 in PBS for 15 min at room temperature. After being washed three times with PBS, the cells were incubated with HCV-infected patient's serum for 1 hr, followed by incubation with FITC-conjugated goat anti-human IgG (MBL, Nagoya, Japan). The cells were counterstained with Hoechst 33342 (Molecular Probes, Eugene, OR, USA) for 5 min and HCV-infected cells were counted under a BZ-9000 fluorescence microscope (Keyence, Osaka, Japan).

Cytotoxicity assay

The cytotoxicity of the samples was assessed by WST-1 assay as described previously with a slight modification (27). In brief, Huh7.5 cells in 96-well plates were treated with serial dilutions of the samples or 0.1% DMSO as a control for 48 hr. At the end of the treatment, 10 μL of WST-1 reagent (Roche, Mannheim, Germany) was added to each well and the cells cultured for 1 hr. The WST-1 reagent is absorbed by the cells and converted to formazan by mitochondrial dehydrogenases. The amount of formazan, which correlates with the number of living cells, was determined by measuring the absorbance of each well using a microplate reader at 450 and 630 nm. Percent cell viability compared to the control was calculated for each dilution of the samples and CC_{50} were determined.

Immunoblotting

Cells were lysed with an SDS sample buffer, after which equal amounts of protein were subjected to SDS–polyacrylamide gel electrophoresis and transferred onto a polyvinylidene difluoride membrane (Millipore, Bedford, MA, USA), as described previously (28, 29). The membranes were incubated with the respective primary

antibodies. The primary antibodies used were mouse monoclonal antibodies against HCV NS3 and GAPDH (Millipore). Horseradish peroxidase-conjugated goat anti-mouse immunoglobulin (Invitrogen) was used to visualize the respective proteins by means of an enhanced chemiluminescence detection system (ECL; GE Healthcare, Buckinghamshire, UK).

Real-time quantitative RT-PCR

Real-time quantitative RT-PCR was performed as described previously (28, 29). In brief, total RNA was extracted from the cells using a ReliaPrep RNA cell miniprep system (Promega, Madison, WI, USA) according to the manufacturer's instructions. One microgram of total RNA was reverse transcribed using a GoScript Reverse Transcription system (Promega) with random primers and subjected to real-time quantitative PCR analysis using SYBR Premix Ex Taq (TaKaRa, Kyoto, Japan) in a MicroAmp 96-well reaction plate and an ABI PRISM 7500 system (Applied Biosystems, Foster City, CA, USA). The HCV-specific primers to amplify an NS5A region of the viral genome were 5′-AGACGTATTGAGGTCCATGC-3′ (sense) and 5′-CCGCAGCGACGGTGCTGATAG-3′ (antisense). Human GAPDH gene expression was measured using primers 5′-GCCATCAATGACCCCTTCATT-3′ (sense) and 5′-TCTCGCTCCTGGAAGATGG-3′, which served as an internal control.

RESULTS

Anti-HCV activity of a methanol extract and sub-fractions of *G. uralensis* roots

First, we examined a crude methanol extract of *G. uralensis* roots for anti-HCV activity using the HCV J6/JFH1-P47 strain and Huh7.5 cells. The IC_{50} and CC_{50} values of the crude methanol extract were 20.0 and 300 μg/mL, respectively, the selectivity indexes (SI: CC_{50}/IC_{50}) being 15 (Table 1). We further partitioned the methanol extract using different solvents and found that the anti-HCV activity was concentrated into a chloroform partition, whose IC_{50} and CC_{50} were 8.0 and 93 μg/mL, respectively, the SI being 11.6.

Table 1. Anti-HCV activity (IC_{50}), cytotoxicity (CC_{50}) and selectivity index (SI) of extracts of *G. uralensis* roots

Sample	IC_{50} (μg/mL)	CC_{50} (μg/mL)	SI
Methanol extract	20.0	300	15.0
Chloroform partition	8.0	93	11.6
n-butanol partition	17.5	250	14.3
Water partition	95.0	>500	>5.3

Table 2. Anti-HCV activity (IC_{50}), cytotoxicity (CC_{50}) and selectivity index (SI) of recycling HPLC fractions of chloroform partition of *G. uralensis* roots

Sample	IC_{50} (μg/mL)	CC_{50} (μg/mL)	SI
Fraction 1	>30	>30	na
Fraction 2	>30	>30	na
Fraction 3	>30	>30	na
Fraction 4	>30	>30	na
Fraction 5	20	>30	>1.5
Fraction 6	2.9	65	22
Fraction 7	3.6	40	11
Fraction 8	2.9	40	14
Fraction 9	2.9	>70	>24
Fraction 10	4.9	>70	>14

na, not applicable.

Next, we sub-fractionated the chloroform partition by using recycling HPLC and examined the sub-fractions for anti-HCV activity. We found significant anti-HCV activity with fractions 6–10, IC_{50} ranging between 2.9 and 4.9 μg/mL (Table 2). We further tried to purify a major component(s) in fractions 6–10 by using recycling HPLC: we identified glycycoumarin (30), glycyrin (31), glycyrol (32) and liquiritigenin (33) by NMR spectrum analysis (data not shown).

Anti-HCV activity of *G. uralensis*-derived purified compounds and related chemical compounds obtained from other *Glycyrrhiza* species

We then examined the purified compounds obtained from the *G. uralensis* extracts (glycycoumarin, glycyrin, glycyrol and liquiritigenin) and other *Glycyrrhiza*-derived chemical compounds, such as glycyrrhizin and its derivatives. We found that glycyrrhizin (glycyrrhizic acid) and its monoammonium salt (glycyrrhizic acid monoammonium), the latter being more water-soluble than the former, possessed only marginal anti-HCV activity, IC_{50} values being 180 and 320 μg/mL, respectively (Table 3). The aglycone of glycyrrhizin, glycyrrhetinic acid, showed more significant anti-HCV activity than did glycyrrhizin, its IC_{50} being 40 μg/mL. It should be noted that their anti-HCV activities were weaker than those of the recycling HPLC fractions 6–10 of the *G. uralensis* extract. The monoglucuronide form of glycyrrhizin, glycyrrhetic acid 3-*O*-glucuronide, did not show significant anti-HCV activity at the concentration tested. These results suggest that another compound(s) in fractions 6–10 was responsible for the anti-HCV activity. Two other saponins tested in this study, licorice-saponins G2 and H2, did not show detectable anti-HCV activity. On the other hand, coumarins, such as

Table 3. Anti-HCV activity (IC_{50}), cytotoxicity (CC_{50}) and selectivity index (SI) of *G. uralensis*- and other *Glycyrrhiza* spp-derived compounds

Sample	IC_{50} (μg/mL)	CC_{50} (μg/mL)	SI
Triterpenoids			
Glycyrrhizin	180	560	3.1
Glycyrrhizic acid monoammonium	320	690	2.2
Glycyrrhetic acid 3-O-glucuronide	>30‡	>30	na
Glycyrrhetinic acid	40.0	77.4	1.9
Licorice-saponin G2	>30‡	>30	na
Licorice-saponin H2	>30‡	>30	na
Coumarins			
Glycycoumarin (isolated)	8.8	69.0	7.8
Glycyrin (isolated)	7.2	25.0	3.5
Glycyrol (isolated)	4.6	35.5	7.7
Flavonoids			
Flavanones			
Liquiritin	75.0	570	7.6
Liquiritigenin	16.4	125	7.6
Chalcones			
Isoliquiritigenin	3.7	11.0	3.0
Licochalcone A†	2.5	20.0	8.0
Isoflavan			
Glabridin†	6.2	22.7	3.7

†Not detected in *G. uralensis* (34). ‡No detectable HCV inhibition at 30 μg/mL. na, not applicable.

glycycoumarin, glycyrin and glycyrol, which were isolated in this study (purity >90%) from the *G. uralensis* extracts, showed potent anti-HCV activity, IC_{50} being 4.6–8.8 μg/mL. Liquiritigenin, which was also isolated from the *G. uralensis* extracts, showed weaker anti-HCV activity than the coumarins. Also, isoliquiritigen, licochalcone A and glabridin exhibited potent anti-HCV activity, their IC_{50} being 3.7, 2.5 and 6.2 μg/mL, respectively. It should be noted that licochalcone A and glabridin have been reported to be absent in *G. uralensis* but present in *G. inflata* and *G. glabra* (34).

Mode-of-action of *G. uralensis*-derived isolated compounds and related compounds obtained from other *Glycyrrhiza* species

To determine whether the anti-HCV effects of the compounds of *Glycyrrhiza* species are exerted on the entry or post-entry stage, we performed the following time-of-addition experiments.

1. HCV was mixed with a test compound and the mixture inoculated into the cells. After virus adsorption for 2 hr, the residual virus and test sample were removed and the cells re-fed with fresh medium without the test sample for 46 hr. This experiment examines the antiviral effect at the entry step.
2. HCV was inoculated into the cells in the absence of a test sample. After virus adsorption for 2 hr, the residual virus was removed and the cells treated with the test samples for 46 hr. This experiment examines the antiviral effect at the post-entry step.
3. As a positive control, HCV mixed with the test sample was inoculated into the cells. After virus adsorption for 2 hr, the residual virus and test sample were removed and the cells treated with the test samples for 46 hr.

Table 4. Mode-of-action analysis of anti-HCV activities of *G. uralensis*- and other *Glycyrrhiza* spp.-derived compounds

Compound	Conc. (mg/mL)†	Anti-HCV activity (% inhibition) During‡	After‡	During & after‡
Chloroform partition	30	28.6	100	100
Glycycoumarin	20	16.7	100	100
Glycyrin	15	18.4	98.3	99.6
Glycyrol	10	21.3	100	100
Liquiritigenin	30	15.5	90.0	87.2
Isoliquiritigenin	8	14.1	91.0	82.5
Licochalcone A	5	0	94.4	93.8
Glabridin	12	0	91.0	93.8

†The concentrations of each compound used were 2 × IC_{50}. ‡Treatment with the compound was administered only during, only after or both during and after virus inoculation.

We found that all the *Glycyrrhiza* species-derived compounds as well as the chloroform partition of the *G. uralensis* extract exerted their antiviral effects after virus inoculation (Table 4). These results suggest that all the anti-HCV compounds of *Glycyrrhiza* species tested in this study, namely, glycycoumarin, glycyrin, glycyrol, liquiritigenin, isoliquiritigenin, licochalcone A and glabridin, as well as the chloroform extract, act primarily at the post-entry step.

Inhibition of HCV RNA replication and HCV protein synthesis by glycycoumarin, glycyrin, and glycyrol obtained from *G. uralensis*

To further confirm that *G. uralensis*-derived compounds exert their anti-HCV activities at the post-entry step, Huh7.5 cells were inoculated with HCV for 2 hr, followed by treatment with each of compounds for 1–2 days. The results obtained clearly demonstrated that glycycoumarin, glycyrin and glycyrol inhibit HCV RNA replication, resulting in decreased HCV protein

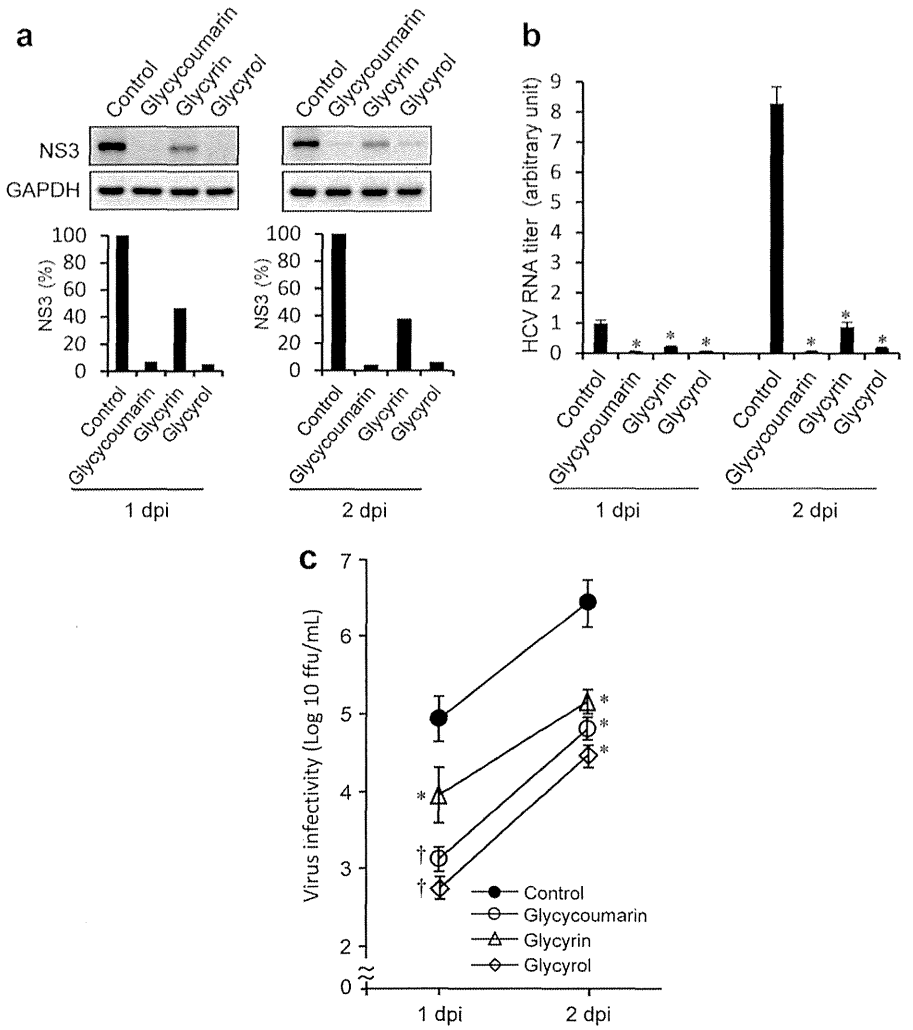

Fig. 1. Effects of glycycoumarin, glycyrin and glycyrol isolated from *G. uralensis* on HCV RNA replication and protein synthesis. (a) Huh 7.5 cells infected with HCV J6/JFH1 and treated with either glycycoumarin (20 μg/mL), glycyrin (15 μg/mL), glycyrol (10 μg/mL) or left untreated were subjected to western blot analysis using monoclonal antibody against the HCV NS3 protein at 1 and 2 days post-infection. GAPDH served as an internal control to verify equal amounts of sample loading. Signal intensities of NS3 were normalized to the corresponding GAPDH signal. (b) Amounts of HCV RNA in the cells described in (a) were measured by real-time quantitative RT-PCR analysis. These amounts were normalized to GAPDH mRNA expression. Data represent means ± SEM of data from two independent experiments. The value for the untreated control at 1 day post-infection is arbitrarily expressed as 1.0. $^{*}P < 0.001$, compared with the control. (c) Amounts of HCV infectious particles in the supernatants of the cultures described in (a) and (b) were determined: data for glycycoumarin, glycyrin, glycyrol and the untreated control are shown. Data represent means ± SEM of data from two independent experiments. $^{*}P < 0.05$; $^{\dagger}P < 0.01$, compared with the untreated control; dpi, days post infection.

synthesis as demonstrated by both real-time quantitative RT-PCR and immunoblotting analyses (Fig. 1a, b). We also confirmed that production of HCV infectious particles is inhibited by glycycoumarin, glycyrin and glycyrol at 1 and 2 days post-infection (Fig 1c).

DISCUSSION

Glycyrrhiza species possess a variety of bioactive compounds, such as: (i) triterpenoids, for example, glycyrrhizin, glycyrrhetic acid 3-*O*-glucuronide, glycyrrhetinic acid and various licorice-saponins; (ii) coumarins, for example, glycycoumarin, glycyrin and glycyrol; (iii) flavanones, for example, liquiritin and liquiritigenin; (iv) chalcones, for example, isoliquiritigenin and licochalcone; (v) isoflavans, for example, glabridin; (vi) stilbenoids, for example, dihydrostilbenes; and other miscellaneous compounds (11). In this connection, flavanones, chalcones and isoflavans are members of flavonoids.

Glycyrrhizin is the major constituent of *Glycyrrhiza* species, representing 1–9% of the total (14). Glycyrrhizin and other compounds isolated from *Glycyrrhiza* species reportedly possess antiviral activity against a variety of viruses (11–15). With regard to HCV, it was recently reported that glycyrrhizin inhibits HCV infection in Huh-7 cells (19, 20). On the other hand, controversial observations have been reported in clinical settings; namely, that glycyrrhizin has no significant effect on amounts of HCV RNA whereas it reduces serum alanine aminotransferase concentrations in HCV-infected patients (16, 17). These apparently contradictory findings might be explained by a membrane-stabilizing effect of glycyrrhizin; clear evidence for antiviral activity of glycyrrhizin is still lacking (10). In the present study, we observed that glycyrrhizin and glycyrrhizic acid monoammonium showed only marginal anti-HCV activity (Table 3). Glycyrrhetinic acid showed significant anti-HCV activity. However, their anti-HCV activities were significantly weaker than that of the HPLC fractions obtained from *G. uralensis* extract. On the other hand, we found that certain coumarins, such as glycycoumarin, glycyrin and glycyrol, and a flavanone, liquiritigenin, isolated from *G. uralensis*, as well as other compounds contained in *Glycyrrhiza* species, possess potent anti-HCV activities. Mode-of-action analysis revealed that all the *Glycyrrhiza*-derived anti-HCV compounds tested act primarily at the post-entry step. Consistent with our observations, other researchers have also reported that two flavonoids, isoliquiritigenin and glycycoumarin, extracted from *Glycyrrhizae radix*, either *G. uralensis* or *G. glabra*, inhibit replication of an HCV subgenomic RNA replicon *in vitro* (35). The IC_{50} values of isoliquiritigenin and glycycoumarin against HCV subgenomic replicon were 6.2 and 15.5 μg/mL, respectively. On the other hand, to the best of our knowledge, there are no published reports so far regarding anti-HCV activities of glycyrin and glycyrol. It has been reported that glycyrin, which is known to possess peroxisome proliferator-activated receptor-γ ligand-binding activity, shows antibacterial activity against *Streptococcus pyogenes*, *Haemophilus influenzae* and *Moraxella catarrhalis* (36–38). Glycyrol reportedly exerts anti-inflammatory effects by binding to calcineurin to inhibit its activity (39, 40). However, the possible antimicrobial activity of glycyrol has not been reported. Further study is needed to elucidate the detailed mechanism of anti-HCV activities of glycyrin and glycyrol, and also possible antiviral activities against viruses other than HCV.

In conclusion, our results suggest that glycycoumarin, glycyrin, glycyrol and liquiritigenin isolated from *G. uralensis*, as well as isoliquiritigenin, licochalcone A and glabridin, would be good candidates for seed compounds to develop antivirals against HCV.

ACKNOWLEDGMENTS

The authors are grateful to Dr. C. M. Rice (Rockefeller University, New York, NY, USA) for providing Huh7.5 cells and pFL-J6/JFH1. This study was supported in part by Science and Technology Research Partnerships for Sustainable Development (SATREPS) from Japan Science and Technology Agency (JST) and Japan International Cooperation Agency (JICA). This study was also carried out as part of the Japan Initiative for Global Research Network on Infectious Diseases (J-GRID), Ministry of Education, Culture, Sports, Science and Technology, Japan.

DISCLOSURE

The authors have no conflicts of interest to declare.

REFERENCES

1. Gottwein J.M., Scheel T.K., Jensen T.B., Lademann J.B., Prentoe J.C., Knudsen M.L., Hoegh A.M., Bukh J. (2009) Development and characterization of hepatitis C virus genotype 1–7 cell culture systems: role of CD81 and scavenger receptor class B type I and effect of antiviral drugs. *Hepatology* **49**: 364–77.
2. Smith D.B., Bukh J., Kuiken C., Muerhoff A.S., Rice C.M., Stapleton J.T., Simmonds P. (2013) Expanded classification of hepatitis C Virus into 7 genotypes and 67 Subtypes: updated criteria and assignment web resource. *Hepatology* **59**: 318–27.
3. Moradpour D., Penin F., Rice C.M. (2007) Replication of hepatitis C virus. *Nat Rev Microbiol* **5**: 453–6.
4. Shoji I., Deng L., Hotta H. (2011) Molecular mechanism of hepatitis C virus-induced glucose metabolic disorders. *Front Microbiol* **2**: 278.
5. Arzumanyan A., Reis H.M., Feitelson M.A. (2013) Pathogenic mechanisms in HBV- and HCV-associated hepatocellular carcinoma. *Nat Rev Cancer* **13**: 123–35.
6. Shepard C.W., Finelli L., Alter M.J. (2005) Global epidemiology of hepatitis C virus infection. *Lancet Infect Dis* **5**: 558–67.
7. Mohd Hanafiah K., Groeger J., Flaxman A.D., Wiersma S.T. (2013) Global epidemiology of hepatitis C virus infection: new estimates of age-specific antibody to HCV seroprevalence. *Hepatology* **57**: 1333–42.
8. Calland N., Dubuisson J., Rouille Y., Seron K. (2012) Hepatitis C virus and natural compounds: a new antiviral approach? *Viruses* **4**: 2197–217.
9. Ploss A., Dubuisson J. (2012) New advances in the molecular biology of hepatitis C virus infection: towards the identification of new treatment targets. *Gut* **61** (Suppl 1): i25–35.
10. Stickel F., Schuppan D. (2007) Herbal medicine in the treatment of liver diseases. *DigLiver Dis* **39**: 293–304.
11. Asl M.N., Hosseinzadeh H. (2008) Review of pharmacological effects of *Glycyrrhiza* sp. and its bioactive compounds. *Phytother Res* **22**: 709–24.

12. Pompei R., Flore O., Marccialis M.A., Pani A., Loddo B. (1979) Glycyrrhizic acid inhibits virus growth and inactivates virus particles. *Nature* **281**: 689–90.
13. Cinatl J., Morgenstern B., Bauer G., Chandra P., Rabenau H., Doerr H.W. (2003) Glycyrrhizin, an active component of liquorice roots, and replication of SARS-associated coronavirus. *Lancet* **361**: 2045–6.
14. Fiore C., Eisenhut M., Krausse R., Ragazzi E., Pellati D., Armanini D., Bielenberg J. (2008) Antiviral effects of Glycyrrhiza species. *Phytother Res* **22**: 141–8.
15. Wang J., Chen X., Wang W., Zhang Y., Yang Z., Jin Y., Ge H.M., Li E., Yang G. (2013) Glycyrrhizic acid as the antiviral component of *Glycyrrhiza uralensis* Fisch. against coxsackievirus A16 and enterovirus 71 of hand foot and mouth disease. *J Ethnopharmacol* **147**: 114–21.
16. van Rossum T.G., Vulto A.G., Hop W.C., Brouwer J.T., Niesters H.G., Schalm S.W. (1999) Intravenous glycyrrhizin for the treatment of chronic hepatitis C: a double-blind, randomized, placebo-controlled phase I/II trial. *J Gastroenterol Hepatol* **14**: 1093–9.
17. Orlent H., Hansen B.E., Willems M., Brouwer J.T., Huber R., Kullak-Ublick G.A., Gerken G., Zeuzem S., Nevens F., Tielemans W.C., Zondervan P.E., Lagging M., Westin J., Schalm S.W. (2006) Biochemical and histological effects of 26 weeks of glycyrrhizin treatment in chronic hepatitis C: a randomized phase II trial. *J Hepatol* **45**: 539–46.
18. Korenaga M., Hidaka I., Nishina S., Sakai A., Shinozaki A., Gondo T., Furutani T., Kawano H., Sakaida I., Hino K. (2011) A glycyrrhizin-containing preparation reduces hepatic steatosis induced by hepatitis C virus protein and iron in mice. *Liver Int* **31**: 552–60.
19. Ashfaq U.A., Masoud M.S., Nawaz Z., Riazuddin S. (2011) Glycyrrhizin as antiviral agent against hepatitis C virus. *J Transl Med* **9**: 112.
20. Matsumoto Y., Matsuura T., Aoyagi H., Matsuda M., Hmwe S.S., Date T., Watanabe N., Watashi K., Suzuki R., Ichinose S., Wake K., Suzuki T., Miyamura T., Wakita T., Aizaki H. (2013) Antiviral activity of glycyrrhizin against hepatitis C virus in vitro. *PLoS ONE* **8**: e68992.
21. Lindenbach B.D., Evans M.J., Syder A.J., Wolk B., Tellinghuisen T.L., Liu C.C., Maruyama T., Hynes R.O., Burton D.R., McKeating J.A., Rice C.M. (2005) Complete replication of hepatitis C virus in cell culture. *Science* **309**: 623–6.
22. Bungyoku Y., Shoji I., Makine T., Adachi T., Hayashida K., Nagano-Fujii M., Ide Y., Deng L., Hotta H. (2009) Efficient production of infectious hepatitis C virus with adaptive mutations in cultured hepatoma cells. *J Gen Virol* **90**: 1681–9.
23. Li S.Y., Fuchino H., Kawahara N., Sekita S., Satake M. (2002) New phenolic constituents from Smilax bracteata. *J Nat Prod* **65**: 262–6.
24. Fuchino H., Sekita S., Mori K., Kawahara N., Satake M., Kiuchi F. (2008) A new leishmanicidal saponin from Brunfelsia grandiflora. *Chem Pharm Bull* **56**: 93–6.
25. Fuchino H., Kawano M., Mori-Yasumoto K., Sekita S., Satake M., Ishikawa T., Kiuchi F., Kawahara N. (2010) *In vitro* leishmanicidal activity of benzophenanthridine alkaloids from *Bocconia pearcei* and related compounds. *Chem Pharm Bull* **58**: 1047–50.
26. Fuchino H., Daikonya A., Kumagai T., Goda Y., Takahashi Y., Kawahara N. (2013) Two new labdane diterpenes from fresh leaves of *Leonurus japonicus* and their degradation during drying. *Chem Pharm Bull* **61**: 497–503.
27. Deng L., Adachi T., Kitayama K., Bungyoku Y., Kitazawa S., Ishido S., Shoji I., Hotta H. (2008) Hepatitis C virus infection induces apoptosis through a Bax-triggered, mitochondrion-mediated, caspase 3-dependent pathway. *J Virol* **82**: 10375–8.
28. Deng L., Shoji I., Ogawa W., Kaneda S., Soga T., Jiang D.P., Ide Y.H., Hotta H. (2011) Hepatitis C virus infection promotes hepatic gluconeogenesis through an NS5A-mediated, FoxO1-dependent pathway. *J Virol* **85**: 8556–68.
29. Wahyuni T.S., Tumewu L., Permanasari A.A., Apriani E., Adianti M., Rahman A., Widyawaruyanti A., Lusida M.I., Fuad A., Soetjipto D., Nasronudin D., Fuchino H., Kawahara N., Shoji I., Deng L., Aoki C., Hotta H. (2013) Antiviral activities of Indonesian medicinal plants in the East Java region against hepatitis C virus. *Virol J* **10**: 259.
30. Demizu S., Kajiyama K., Takahashi K., Hiraga Y., Yamamoto S., Tamura Y., Okada K., Kinoshita T. (1988) Antioxidant and antimicrobial constituents of licorice: isolation and structure elucidation of a new benzofuran derivative. *Chem Pharm Bull* **36**: 3474–9.
31. Kinoshita T., Saitoh T., Shibata S. (1978) A new 3-arylcoumarin from licorice root. *Chem Pharm Bull* **26**: 135–40.
32. Shiozawa T., Urata S., Kinoshita T., Saitoh T. (1989) Revised structures of glycyrol and isoglycyrol, constituents of the root of Glycyrrhiza uralensis. *Chem Pharm Bull* **37**: 2239–40.
33. Chokchaisiri R., Suaisom C., Sriphota S., Chindaduang A., Chuprajob T., Suksamrarn A. (2009) Bioactive flavonoids of the flowers of Butea monosperma. *Chem Pharm Bull* **57**: 428–32.
34. Kondo K., Shiba M., Nakamura R., Morota T., Shoyama Y. (2007) Constituent properties of licorices derived from *Glycyrrhiza uralensis*, *G. glabra*, or *G. inflata* identified by genetic information. *Biol Pharm Bull* **30**: 1271–7.
35. Sekine-Osajima Y., Sakamoto N., Nakagawa M., Itsui Y., Tasaka M., Nishimura-Sakurai Y., Chen C.H., Suda G., Mishima K., Onuki Y., Yamamoto M., Maekawa S., Enomoto N., Kanai T., Tsuchiya K., Watanabe M. (2009) Two flavonoids extracts from *Glycyrrhizae radix* inhibit *in vitro* hepatitis C virus replication. *Hepatol Res* **39**: 60–9.
36. Mae T., Kishida H., Nishiyama T., Tsukagawa M., Konishi E., Kuroda M., Mimaki Y., Sashida Y., Takahashi K., Kawada T., Nakagawa K., Kitahara M. (2003) A licorice ethanolic extract with peroxisome proliferator-activated receptor-gamma ligand-binding activity affects diabetes in KK-Ay mice, abdominal obesity in diet-induced obese C57BL mice and hypertension in spontaneously hypertensive rats. *J Nutr* **133**: 3369–77.
37. Kuroda M., Mimaki Y., Sashida Y., Mae T., Kishida H., Nishiyama T., Tsukagawa M., Konishi E., Takahashi K., Kawada T., Nakagawa K., Kitahara M. (2003) Phenolics with PPAR-gamma ligand-binding activity obtained from licorice (*Glycyrrhiza uralensis* roots) and ameliorative effects of glycyrin on genetically diabetic KK-A(y) mice. *Bioorg Med Chem Lett* **13**: 4267–72.
38. Tanaka Y., Kikuzaki H., Fukuda S., Nakatani N. (2001) Antibacterial compounds of licorice against upper airway respiratory tract pathogens. *J Nutr Sci Vitaminol* **47**: 270–3.
39. Peng L., Qi Y., Wu H., Wei Q. (2011) Interaction of glycyrol with calcineurin A studied by spectroscopic methods and docking. *IUBMB Life* **63**: 14–20.
40. Shin E.M., Zhou H.Y., Guo L.Y., Kim J.A., Lee S.H., Merfort I., Kang S.S., Kim H.S., Kim S., Kim Y.S. (2008) Anti-inflammatory effects of glycyrol isolated from *Glycyrrhiza uralensis* in LPS-stimulated RAW264. 7 macrophages. *Int Immunopharmacol* **8**: 1524–32.

ANTIOXIDANTS & REDOX SIGNALING
Volume 21, Number 1, 2014

DOI: 10.1089/ars.2013.5381

Discoveries

ORIGINAL RESEARCH COMMUNICATION

Nitrosative Stress Induces Peroxiredoxin 1 Ubiquitination During Ischemic Insult *via* E6AP Activation in Endothelial Cells Both *In Vitro* and *In Vivo*

Rong-Rong Tao,[1,*] Huan Wang,[1,*] Ling-Juan Hong,[1] Ji-Yun Huang,[1] Ying-Mei Lu,[2] Mei-Hua Liao,[1] Wei-Feng Ye,[1,3] Nan-Nan Lu,[1] Dan-Yan Zhu,[1] Qian Huang,[4] Kohji Fukunaga,[5] Yi-Jia Lou,[1] Ikuo Shoji,[6] Christopher Stuart Wilcox,[7] En-Yin Lai,[4,7] and Feng Han[1]

Abstract

Aims: Although there is accumulating evidence that increased formation of reactive nitrogen species in cerebral vasculature contributes to the progression of ischemic damage, but the underlying molecular mechanisms remain elusive. Peroxiredoxin 1 (Prx1) can initiate the antioxidant response by scavenging free radicals. Therefore, we tested the hypothesis that Prx1 regulates the susceptibility to nitrosative stress damage during cerebral ischemia *in vitro* and *in vivo*. ***Results:*** Proteomic analysis in endothelial cells revealed that Prx1 was upregulated after stress-related oxygen–glucose deprivation (OGD). Although peroxynitrite upregulated Prx1 rapidly, this was followed by its polyubiquitination within 6 h after OGD mediated by the E3 ubiquitin ligase E6-associated protein (E6AP). OGD colocalized E6AP with nitrotyrosine in endothelial cells. To assess translational relevance *in vivo*, mice were studied after middle cerebral artery occlusion (MCAO). This was accompanied by Prx1 ubiquitination and degradation by the activation of E6AP. Furthermore, brain delivery of a lentiviral vector encoding *Prx1* in mice inhibited blood–brain barrier leakage and neuronal damage significantly following MCAO. ***Innovation and Conclusions:*** Nitrosative stress during ischemic insult activates E6AP E3 ubiquitin ligase that ubiquitinates Prx1 and subsequently worsens cerebral damage. Thus, targeting the Prx1 antioxidant defense pathway may represent a novel treatment strategy for neurovascular protection in stroke. *Antioxid. Redox Signal.* 21, 1–16.

Introduction

BRAIN MICROVASCULAR ENDOTHELIAL CELLS provide a barrier between the bloodstream and brain that is critical in brain development, maturation, and homeostasis (9, 37). The balance between endothelial cell survival and death is pivotal for brain remodeling and repair (41). Increased cell death of cerebrovascular endothelial cells exacerbates inflammatory, ischemic, and degenerative brain diseases (26). Before a new strategy can be developed to counter these adverse effects of ischemia-induced endothelial dysfunction and neurovascular damage, it is necessary to define the factors responsible for ischemia-induced blood–brain barrier (BBB) damage.

Under conditions of intense oxidative stress, such as ischemia or hypoxia injury, increased generation of nitric oxide (NO) and superoxide ($O_2^{\bullet -}$) results in the formation of peroxynitrite ($ONOO^-$) (50). This is a short-lived highly reactive oxidant that attacks and inactivates many proteins. Specifically, $ONOO^-$ irreversibly inactivates prostacyclin

[1]Institute of Pharmacology, Toxicology and Biochemical Pharmaceutics, Zhejiang University, Hangzhou, China.
[2]School of Medicine, Zhejiang University City College, Hangzhou, Zhejiang, China.
[3]The Children's Hospital, Zhejiang University School of Medicine, Hangzhou, China.
[4]Department of Physiology, Zhejiang University School of Medicine, Hangzhou, China.
[5]Department of Pharmacology, Graduate School of Pharmaceutical Sciences, Tohoku University, Sendai, Japan.
[6]Division of Microbiology, Center for Infectious Diseases, Kobe University Graduate School of Medicine, Kobe, Japan.
[7]Hypertension, Kidney, and Vascular Research Center, Georgetown University Medical Center, Washington, District of Columbia.
*Both authors contributed equally to this work.

Innovation

Our study is the first demonstration that nitrosative stress initiates the ubiquitination of peroxiredoxin 1 (Prx1) and subsequent disturbance of redox homeostasis in endothelial cells during ischemia-like injury. Our findings further identified E6-associated protein (E6AP) E3 ligase that ubiquitinated Prx1. Thus, repression of peroxynitrite ($ONOO^-$) formation or *E6AP* knockdown dampened the ischemia-induced disturbance of Prx1 defense signaling. Since an active Prx1 was required for optimal neurovascular cell survival, targeting the Prx1 antioxidant defense pathway may represent a novel treatment strategy for neurovascular protection after stroke.

synthase and oxidizes tetrahydrabiopterin to dihydrabiopterin, thereby uncoupling endothelial NO synthase and directing it to generate $O_2^{\bullet -}$ in place of NO. Indeed, endothelial cells are the primary targets of nitrosative stress in cardiovascular disease, stroke, and neurodegenerative disorders (18, 48). Although nitrosative damage to lipids, proteins, and DNA has been implicated in neurovascular damage following cerebral ischemia, the downstream signaling mechanisms remain elusive (13, 16, 17, 29).

Peroxiredoxins (Prxs) are thiol-specific antioxidant enzymes that maintain redox balance under both normal conditions and oxidative stress (6, 7, 10, 28). Although Prx1 is the most abundant and widely distributed member of the mammalian Prxs (23, 24) and is a recognized peroxide-detoxifying enzyme, its pathophysiological role during brain disease remains unclear (38, 44). Cultured *Prx1*-deficient fibroblasts have decreased proliferation and increased sensitivity to oxidative DNA damage. *Prx1*-deficient mice developed hemolytic anemia caused by increased erythrocytic reactive oxygen species (ROS) (34). Furthermore, mutant Hungtington (*mHtt*) gene expression decreased Prx1 levels and increased its sulfonylation (35).

We tested the hypothesis that Prx1 in endothelial cells in culture and in the brain *in vivo* is a pivotal antioxidant pathway but can be damaged by nitrosative stress during hypoxia or ischemia, thereby exacerbating injury. We report that oxygen/glucose-deprived endothelial cells ubiquitinate Prx1 by nitrosative activation of E3 ubiquitin ligase (E6-associated protein [E6AP]). The outcome is that Prx1 is targeted for degradation leading to cellular redox imbalance and loss of the integrity of the endothelial BBB in mice following ischemia. Repression of $ONOO^-$ formation or *E6AP* knockdown dampened these disturbances of Prx1 defense signaling in endothelial cells. The initial study was made in human umbilical vascular endothelial cells, and key observations were confirmed and extended in human brain microvascular endothelial cells (HBMECs). Thus, our results indicate that Prx1 is a pivotal molecule for the protection of endothelial cells and microvessels from ischemia-induced neurovascular damage both *in vitro* and *in vivo*.

Results

Identification of differentially expressed proteins after oxygen–glucose deprivation in endothelial cells

Two-dimensional gel electrophoresis was performed in EA.hy926 endothelial cells to identify proteins that were differentially expressed between control and oxygen–glucose deprivation (OGD)-treated endothelial cells. Figure 1A shows a silver-stained two-dimensional gel electrophoresis reference map of the OGD-treated endothelial cultures (Fig. 1A, $n=3$, lower) in comparison to the control profile (Fig. 1A, $n=3$, upper). The spots that showed a twofold or greater difference between treatments were further characterized by trypsin digestion and matrix-assisted laser desorption/ionization (MALDI) time-of-flight (TOF) mass spectrometry. Twenty-two different proteins from 36 spots were identified with high confidence (CI % ranging from 97.5% to 100%) (Supplementary Table S1; Supplementary Data are available online at www.liebertpub.com/ars). The identified proteins were classified into functional groups (Supplementary Fig. S1). We selected Prx1 for further study since it was implicated in oxidation–reduction balance and abundantly increased 2.5-fold after OGD treatment (Supplementary Fig. S2A).

Temporal changes of Prx1 protein levels in endothelial cells after OGD

Immunoblotting studies demonstrated a time-dependent increase in Prx1 over 1–6 h followed by a decline after 12 h (Fig. 1B, C). There was a similar pattern of protein levels of heat shock protein 27 (HSP27) (Fig. 1B, C). Molecular chaperones such as HSP27 can defend against protein misfolding after sublethal stressful stimuli (4). Immunocytochemical experiments demonstrated intracellular localization of Prx1 (Fig. 1D), which increased 6 h after OGD treatment in the cytosol of endothelial cells (Fig. 1D, E).

Characterization of OGD-induced Prx1 ubiquitination in endothelial cells

Unexpectedly, our Western blot data demonstrated a continual increase in the density of a broad, high-molecular-weight (>118 kDa) band for Prx1 starting 6 h after OGD treatment (Fig. 2A). A similar increase in a high-molecular-weight band (>118 kDa) was detected following OGD treatment after probing with an anti-ubiquitin antibody (Fig. 2B). The OGD-induced ubiquitination of Prx1 was confirmed and extended in HBMECs (Fig. 3 A, B) and mouse cerebral microvascular endothelial cells (bEnd.3) (Supplementary Fig. S2B).

Inhibition of proteosomal uptake with MG132 or lactacystin also increased the high-molecular-weight isoforms of Prx1 (Fig. 2C and Supplementary Fig. S3). Probing with an anti-Prx1 antibody in ubiquitin immunocomplexes from OGD-treated endothelial cells revealed a predominant band larger than 118 kDa (Fig. 2D and Fig. 3C). OGD-induced ubiquitination of Prx1 was confirmed by the immunoprecipitation of Prx1 followed by immunoblotting with an anti-ubiquitin antibody (Fig. 2E and Fig. 3D). Consistently, Western blot analysis of cell extracts from OGD-treated cells demonstrated that high-molecular-weight conjugates of Prx1 were significantly reduced in *ubiquitin-K48R*-transfected endothelial cells (Fig. 2F and Fig. 3E, F).

The role of Prx1 during proapoptotic cascades after OGD treatment

Proapoptotic proteins were identified by immunoblotting of EA.hy926 cells transfected with either an empty vector or

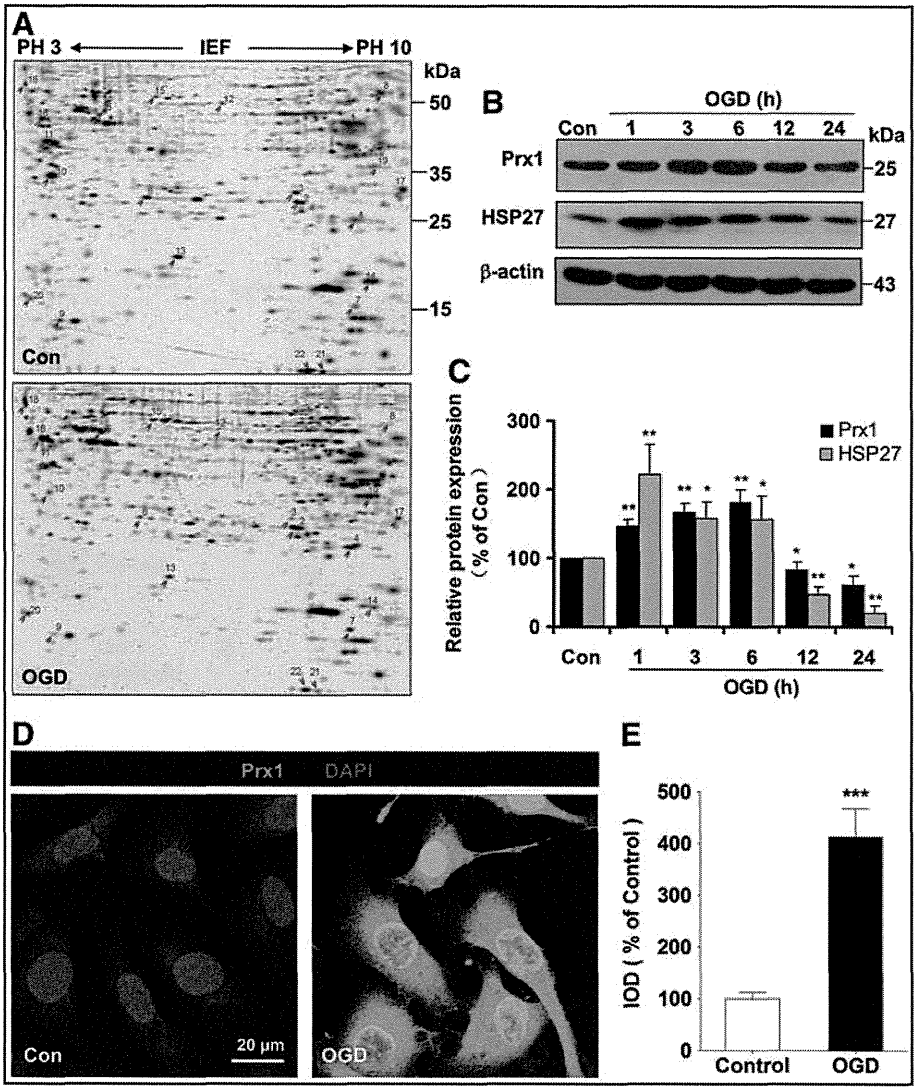

FIG. 1. The proteomic identification of differentially expressed proteins after OGD in endothelial cells. (**A**) Representative silver-stained two-dimensional gel of control and OGD-treated EA.hy926 endothelial cells. Whole proteins (450 μg) were separated on a non-linear pH gradient (3–10) followed by 12% SDS-PAGE. (**B**) Time course of Prx1 and HSP27 protein levels in cell lysates of endothelial cells following OGD. Quantifications of the temporal changes of Prx1 and HSP27 protein levels are shown in (**C**). Immunoblots are representative of three independent experiments. $*p<0.05$; $**p<0.01$ *versus* control. Immunoblotting with an anti-β-actin antibody showed equal amounts of loaded protein in each lane. (**D**) Changes in the immunostaining of Prx1 (green) 6 h after OGD. Subcellular localization of Prx1 was determined by laser confocal microscopy. Data are representative of three independent experiments. Scale bar = 20 μm. (**E**) Quantification of Prx1 immunofluorescence expressed as IOD as described in the Materials and Methods section. $***p<0.001$ *versus* control. IOD, integrated optical density; HSP27, heat shock protein 27; OGD, oxygen–glucose deprivation; Prx1, peroxiredoxin 1; SDS-PAGE, sodium dodecyl sulfate–polyacrylamide gel electrophoresis. To see this illustration in color, the reader is referred to the web version of this article at www.liebertpub.com/ars

a *Prx1* expression vector following OGD insult (Fig. 4). Calnexin is a type I integral endoplasmic reticulum (ER) membrane chaperone involved in folding newly synthesized (glycol) proteins (8). Overexpression of Prx1 significantly inhibited calnexin, PERK, and Ire-1α degradation (Fig. 4A, B) and also inhibited caspase-3 and poly ADP-ribose polymerase (PARP) cleavage (Fig. 4C, D). Exposure of vector-transfected cells to OGD for 6 h decreased the phosphorylation of anti-apoptotic proteins, such as phospho-ERK (Thr202/Tyr204) and phospho-FKHR (Ser256) (forkhead transcription factor Foxo1), and also decreased the protein levels of heme oxygenase-1 (HO-1) but increased the phosphorylation of c-Jun N-terminal kinase (JNK) and P38 (Fig. 4E, F). By contrast, overexpression of *Prx1* after OGD injury resulted in significant upregulation of anti-apoptotic proteins in endothelial cells (Fig. 4E, F). Exposure of vector-transfected cells to OGD for 6 h elevated terminal deoxynucleotidyl transferase dUTP nick end labeling (TUNEL)-positive staining (Fig. 4G, H), whereas overexpression of Prx1 effectively decreased TUNEL staining (Fig. 4G, H). The apoptosis of endothelial cells was determined using flow cytometry with Annexin V-FITC/propidium iodide (PI). In contrast to control cells (2.20%), we found that OGD treatment induced elevation in the fraction of Annexin V/PI-positive cells (49.92%). Moreover, *Prx1* small interfering RNA (siRNA) transduction further exaggerated OGD-induced cell death (Fig. 4I). The present data demonstrate that Prx1 elicits an anti-apoptotic effect after OGD injury in endothelial cells, coinciding with its antioxidant function in the endothelium (31).

E6AP activation contributes to Prx1 stress response after OGD

Since Prx1 has been identified as a novel E6AP-binding protein (33), the present study further elaborates the role of E6AP in ubiquitination of Prx1 during OGD. Representative blots are presented in Figure 5A and show that E6AP was activated following OGD exposure over 1–24 h (Fig. 5A). Similar change of E6AP was confirmed in HBMEC (Supplementary Fig. S4A, B) and bEnd.3 endothelial cells after OGD (Supplementary Fig. S2B). Immunocytochemical analysis of the endothelial cells revealed OGD-induced strong immunoreactivity for E6AP (red fluorescence) that was undetectable in control cells (Fig. 5B–D and Supplementary Fig. S4C, D), which suggests that OGD-induced ubiquitination of Prx1 is associated with E6AP activation.

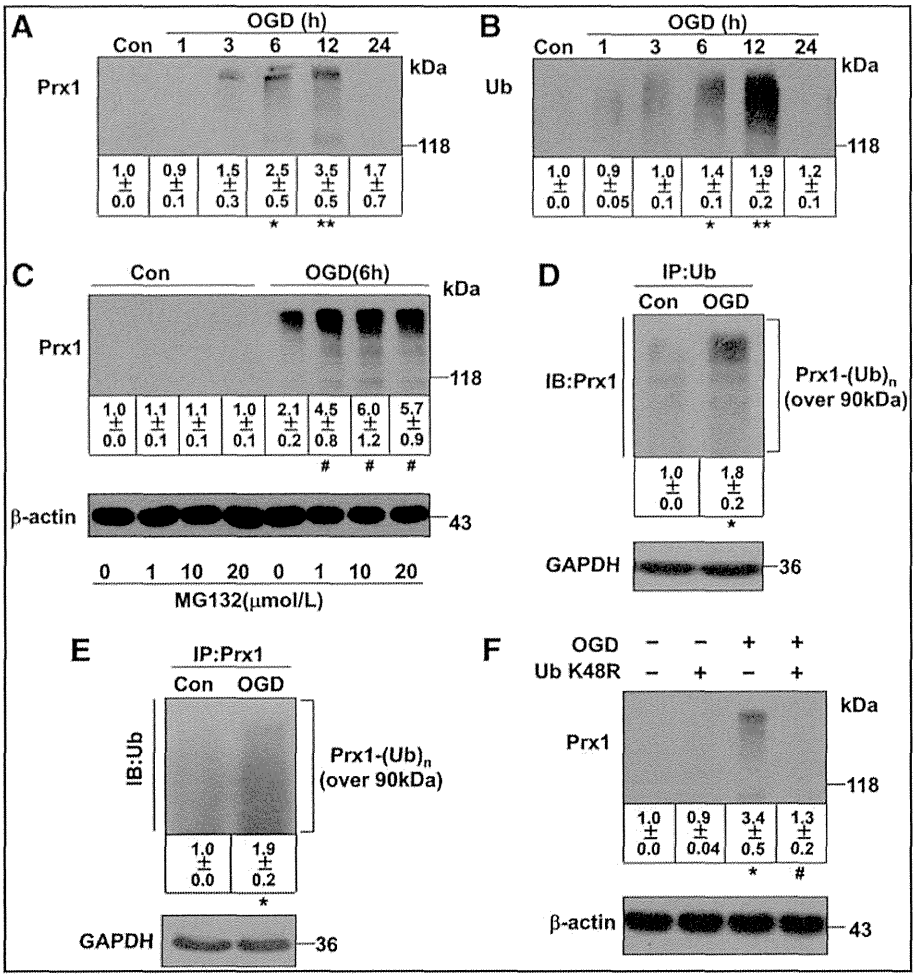

FIG. 2. OGD induces ubiquitination of Prx1 in EA.hy926 endothelial cells. **(A)** Temporal changes in the high-molecular-weight Prx1 isoform were observed in OGD-treated endothelial cells. The accumulated polyubiquitinylated proteins were detected by Western blot analysis with anti-Prx1 antibody. **(B)** Protein ubiquitination status after OGD treatment in endothelial cells. The accumulated multiubiquitinylated proteins were detected by Western blot analysis with an anti-ubiquitin antibody. **(C)** The changes in polyubiquitinated Prx1 were detected following OGD treatment of endothelial cells with or without proteasome inhibitors. The endothelial cells were treated with 1, 10, or 20 μM MG132 or DMSO 30 min before OGD. The cells were then washed, harvested after 6 h OGD, and analyzed for polyubiquitinated Prx1 levels. **(D)** The OGD-induced ubiquitination of Prx1 was detected by the immunoprecipitation of ubiquitin followed by immunoblotting with an anti-Prx1 antibody. **(E)** Immunoprecipitation of Prx1 from cell lysates of OGD-treated endothelial cells followed by blotting with an anti-ubiquitin antibody. **(F)** The ubiquitin K48R mutant decreased OGD-induced Prx1 ubiquitination in endothelial cells. Endothelial cells were cultured and transfected with plasmid DNA encoding the *ubiquitin-K48R* mutant or an empty plasmid, followed by OGD and immunobloting analysis. Immunoblots are representative of three independent experiments. Data are expressed as the percentage of values of control (mean ± SEM). $^{*}p < 0.05$; $^{**}p < 0.01$ *versus* control; $^{\#}p < 0.05$ *versus* OGD.

E6AP and the active-site cysteine-to-alanine-inactivated mutant E6AP were expressed in mammalian *p3869HA-E6AP C-A* cells (22, 46). Here, after 48 h of transfection, siRNA knockdown of *E6AP* (Fig. 5E, F) or transfection with the *E6AP C-A* mutant (Fig. 5G, H) both significantly blunted the ubiquitination of Prx1 in OGD-treated endothelial cells.

Nitrosative stress associated with the Prx1 defensive response after OGD

The $ONOO^-$ donor 3-morpholinosydnonimine (SIN-1) induced early dose-dependent elevation of Prx1 (Supplementary Fig. S5A, B) and Prx1 ubiquitination (Fig. 6A, B) in endothelial cells as detected by immunoblot, accompanied by increased Prx1 immunostaining (Fig. 6C) and activation of E6AP (Fig. 6D). Whereas increased nitrotyrosine immunostaining and E6AP immunoreactivity were observed in OGD-treated cells (Fig. 6E, F), inhibition of $ONOO^-$ with uric acid markedly reduced both nitrotyrosine and E6AP immunostaining after OGD exposure (Fig. 6E). This was confirmed by Western blot (Fig. 6G, H). A similar result was observed in endothelial cells treated with $ONOO^-$ decomposition catalysts (FeTPPS, 1 μM) (Supplementary Fig. S6A, B). E6AP immunoprecipitates from the cell lysates were probed with anti-nitrotyrosine antibody (Fig. 6I). The results

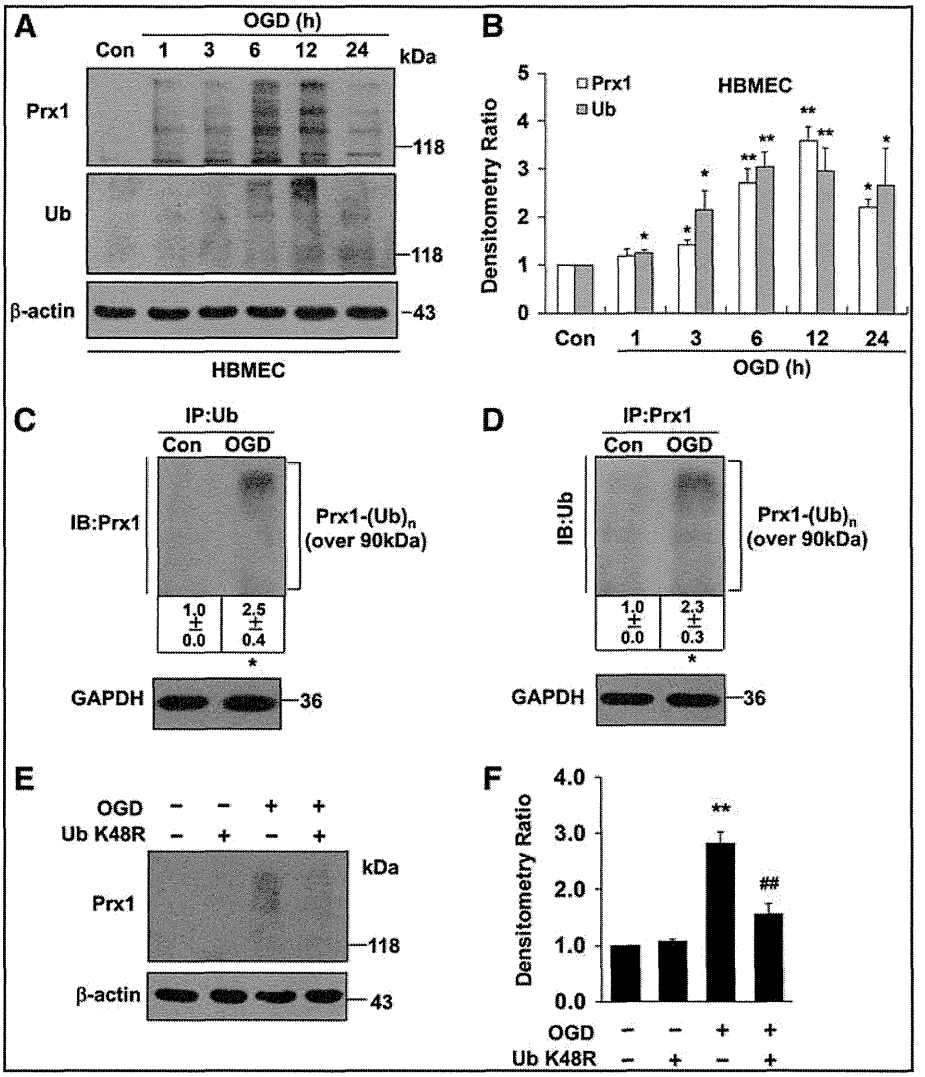

FIG. 3. The ubiquitination of Prx1 in OGD-treated HBMEC. **(A)** The time-dependent change of OGD-induced Prx1 and ubiquitin expression in HBMECs was detected by Western blot. **(B)** Densitometry of the Western blots for **(A)** was normalized by the level of β-actin as an internal control. **(C)** OGD-treated HBMEC endothelial cells were lysed and subjected to immunoprecipitation with antibodies to ubiquitin. The resultant precipitates were then subjected to immunoblot analysis with antibodies to Prx1. **(D)** Immunoprecipitation of Prx1 from lysed HBMEC with or without OGD treatment were collected for immunoblot analysis with ubiquitin antibody. **(E)** The *ubiquitin-K48R* mutant transfection attenuates Prx1 ubiquitination in OGD-treated endothelial cells. HBMEC were cultured and transfected with plasmid DNA encoding the *ubiquitin-K48R* mutant or an empty plasmid. **(F)** Densitometry of the Western blots for **(E)** was normalized by the level of β-actin as an internal control. Immunoblots are representative of three independent experiments. Data are expressed as the percentage of values of control (mean ± SEM). $^{*}p<0.05$; $^{**}p<0.01$ *versus* control; $^{\#\#}p<0.01$ *versus* OGD. HBMEC, human brain microvascular endothelial cell.

demonstrated that the E6AP/nitrotyrosine interaction in OGD-treated endothelial cells was significantly increased. Consistently, OGD-induced tyrosine nitration of E6AP was further confirmed by the immunoprecipitation of nitrotyrosine followed by immunoblotting with an anti-E6AP antibody (Fig. 6J). In addition, Prx1 immunoprecipitates from the lysates were probed with anti-nitrotyrosine antibody demonstrating that OGD did not induce Prx1 protein co-immunoprecipitate with nitrotyrosine (Supplementary Fig. S7). Melatonin blunted the ubiquitination of Prx1 in OGD-treated cells (Supplementary Fig. S8), suggesting that nitrosative stress induced Prx1 ubiquitination during OGD.

E6AP activation contributes to Prx1 stress response in brain microvessels after transient middle cerebral artery occlusion in mice

Since there are limited *in vivo* data on the degradation of Prx1 by ubiquitin ligases in ischemic brain, we used a mouse transient middle cerebral artery occlusion (tMCAO) model for further study. The immunoreactivity for E6AP was observed predominantly in the ipsilateral brain microvessel endothelium 6 h after tMCAO (Fig. 7A-e), accompanied by increased Prx1 immunoreactivity (Fig. 7A-d). A representative Z-stack image is shown in Figure 7B. However, after 24 h, Prx1 was downregulated where E6AP remained upregulated in the brain microvessel endothelium (Fig. 7A, g-i). Ubiquitination of Prx1 was elevated significantly in the brain microvessels 6 h after MCAO (Fig. 7C, D), whereas Prx1 staining was observed in microvessels of sham-operated animals where ubiquitin staining was absent. To further determine E6AP as a key modulator in nitrosative stress-mediated cerebrovascular damage *in vivo*, we stereotaxically delivered a lentivirus carrying mouse sh*E6AP* into the ventricle in mice 2 weeks before MCAO, followed by ischemia and 24 h reperfusion. Western blot analysis showed that lentivirus-mediated cerebral *E6AP* knockdown reduced cerebrovascular damage, which was demonstrated by preventing ischemia-induced dephosphorylation of prosurvival kinases and tight junction proteins breakdown (Fig. 7E–G).

Lentiviral-Prx1 brain transduction protects against neurovascular damage in tMCAO mice

Two weeks after the cerebroventricular injection of a lentiviral-GFP vector encoding mouse *Prx1* (LV-*Prx1*), there was efficient and sustained GFP fluorescence in the brain ventricles (Fig. 8A), cortex (Fig. 8B), hippocampus, and

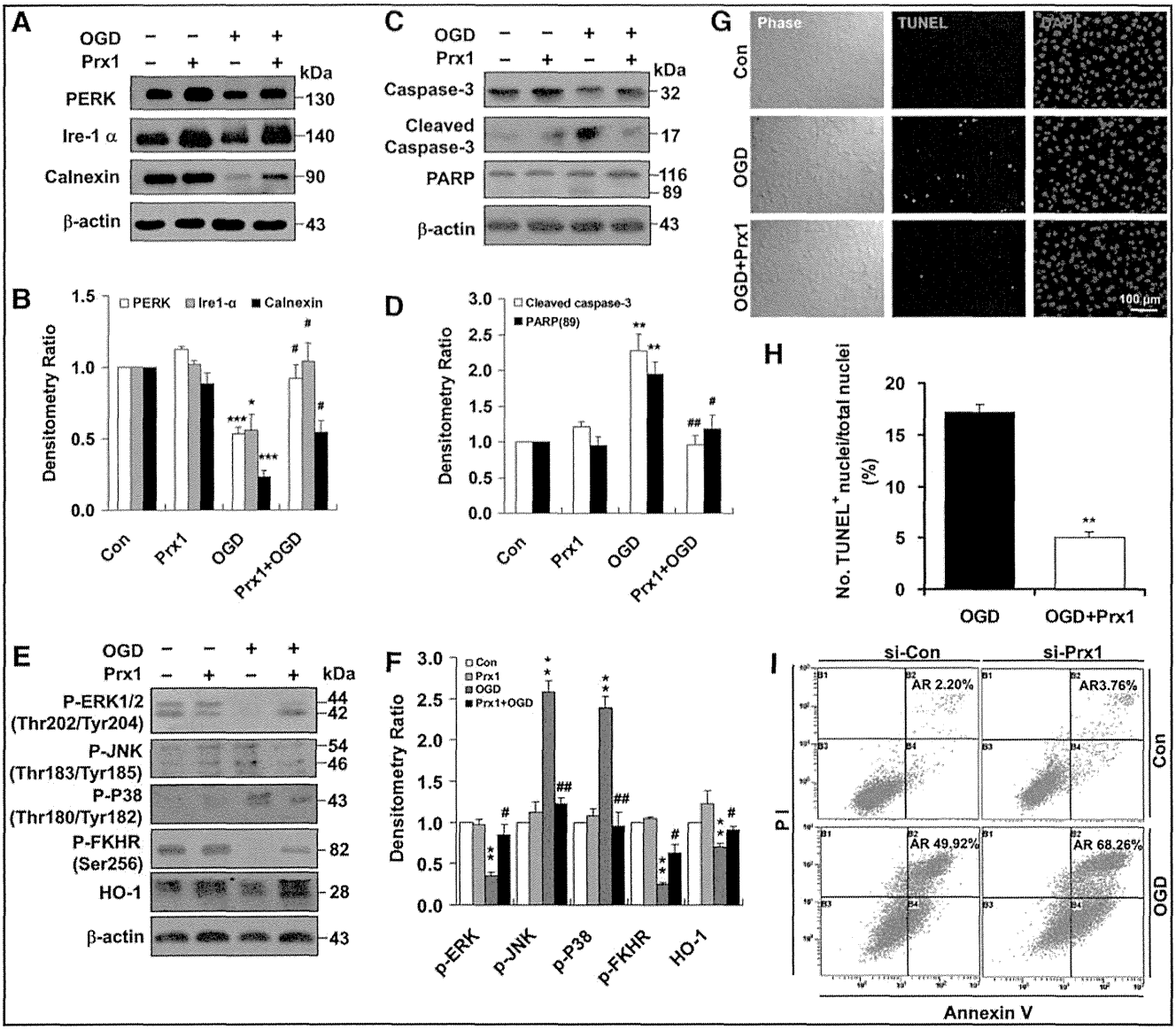

FIG. 4. Role of Prx1 in the OGD-induced apoptotic cascade in endothelial cells. (**A**) The effects of Prx1 on OGD-induced ER stress signaling were determined by immunoblotting. (**B**) Densitometry of Western blots for PERK, Ire-1α, and calnexin levels 6 h after OGD, with or without *Prx1* transfection. Data are expressed as densitometry ratio of control (mean ± SEM). $*p < 0.05$; $***p < 0.001$ *versus* control; $^{\#}p < 0.05$ *versus* OGD. (**C**) The effects of Prx1 overexpression on OGD-induced caspase-3 and PARP levels were evaluated by immunoblotting. EA.hy926 cells were cultured and transfected with plasmid DNA encoding *Prx1* or an empty plasmid using Attractene. (**D**) The quantification data for blots are shown in (**C**). Data are expressed as densitometry ratio of control (mean ± SEM). $**p < 0.01$ *versus* control; $^{\#}p < 0.05$; $^{\#\#}p < 0.01$ *versus* OGD. (**E**) The effects of Prx1 overexpression on OGD-induced protein levels were evaluated by immunoblotting. Cells were transfected with *Prx1* plasmid followed by 6 h of OGD or control stimulation. Cell lysates were prepared and resolved by SDS-PAGE. The proteins were immunoblotted with antibodies against phospho-ERK, phospho-JNK, phospho-P38, phospho-FKHR (Ser256), and HO-1. (**F**) Quantitative analysis of protein levels for (**E**) was performed by densitometry. Data are expressed as densitometry ratio of control (mean ± SEM). $**p < 0.01$ *versus* control; $^{\#}p < 0.05$; $^{\#\#}p < 0.01$ *versus* OGD. (**G**) Changes in apoptosis 6 h after OGD were detected using the TUNEL assay. Double staining was performed for TUNEL (green) and DAPI (blue). The representative images show the increased percentage of TUNEL-positive apoptotic endothelial nuclei (green fluorescence) 6 h after OGD. Scale bar = 100 μm. (**H**) Quantification of TUNEL-positive apoptotic endothelial cells with or without *Prx1* transfection. Apoptosis was dramatically reduced following the overexpression of the *Prx1* gene in endothelial cells after OGD. $**p < 0.01$ *versus* OGD group. (**I**) Representative flow cytometric dot plots of apoptotic cells after OGD with or without *Prx1*siRNA transfection. Cultured EA.hy926 cells were stimulated for 6 h with OGD with or without *Prx1*siRNA transfection. Cells were double-stained with Annexin-V and PI and analyzed by FACS. Immunoblots are representative of three independent experiments. β-Actin was used as the loading control. DAPI, 4′,6-diamidino-2-phenylindole; ER, endoplasmic reticulum; HO-1, heme oxygenase-1; JNK, c-Jun N-terminal kinase; PARP, poly ADP-ribose polymerase; siRNA, small interfering RNA; TUNEL, terminal deoxynucleotidyl transferase dUTP nick end labeling; PI, propidium iodide. To see this illustration in color, the reader is referred to the web version of this article at www.liebertpub.com/ars

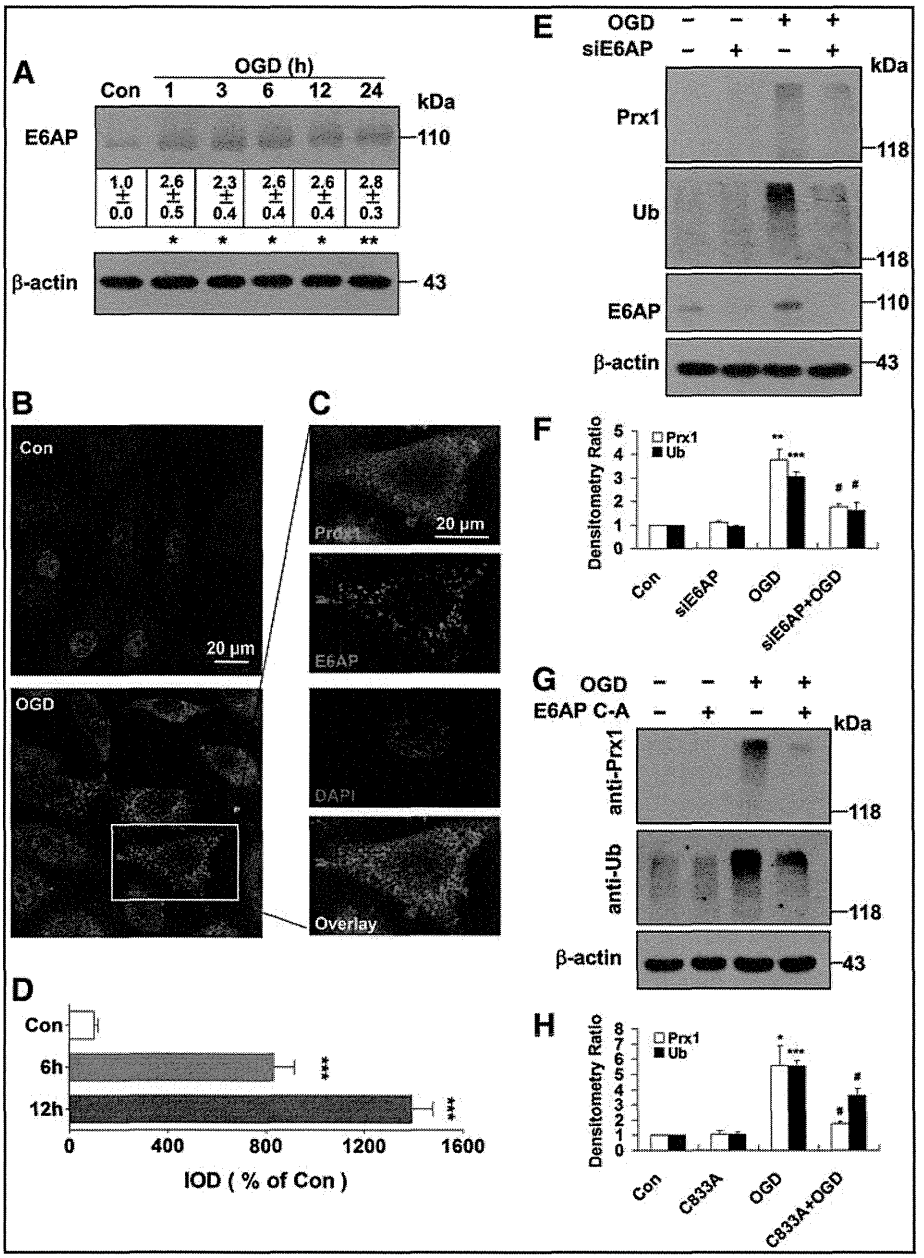

FIG. 5. E6AP activation contributes to the Prx1 stress response after OGD. **(A)** The representative image showing E6AP activation at the indicated time points after OGD treatment. Data are expressed as densitometry ratio of control (mean ± SEM). $*p<0.05$; $**p<0.01$ *versus* control. **(B)** Immunocytochemical analysis of E6AP expression after OGD treatment. Laser confocal microscopy demonstrated low to undetectable levels of E6AP in control cells. **(C)** Higher-magnification image of endothelial staining from the *insets* of **(B)**. DAPI counterstaining indicates nuclear localization (blue). Scale bar = 20 μm. **(D)** Quantification of Prx1 immunofluorescence expressed as integrated optical density (IOD). $***p<0.001$ *versus* control. **(E)** *E6AP* knockdown reduced the OGD-induced formation of multiubiquitinylated proteins. Cells were submitted to *E6AP* knockdown and OGD or the control condition for 6 h. Cell lysates were prepared and resolved by SDS-PAGE. The proteins were immunoblotted with antibodies against Prx1, E6AP, and ubiquitin. **(F)** Quantitative analyses for **(E)** are shown in the bar graph as densitometry ratio of control (mean ± SEM). $**p<0.01$; $***p<0.001$ *versus* control; $^{\#}p<0.05$ *versus* OGD. **(G)** The E6AP$_{C\text{-}A}$ mutant decreased OGD-induced Prx1 ubiquitination in endothelial cells. EA.hy926 cells were cultured and transfected with plasmid DNA encoding the *E6AP*$_{C\text{-}A}$ mutant or an empty plasmid using Attractene. **(H)** Quantitative analysis of protein levels for **(G)** was performed by densitometry. Data are expressed as densitometry ratio of control (mean ± SEM). $*p<0.05$; $***p<0.001$ *versus* control; $^{\#}p<0.05$ *versus* OGD. Immunodetection of β-actin was used as a loading control. Immunoblots are representative of three independent experiments. E6AP, E6-associated protein. To see this illustration in color, the reader is referred to the web version of this article at www.liebertpub.com/ars

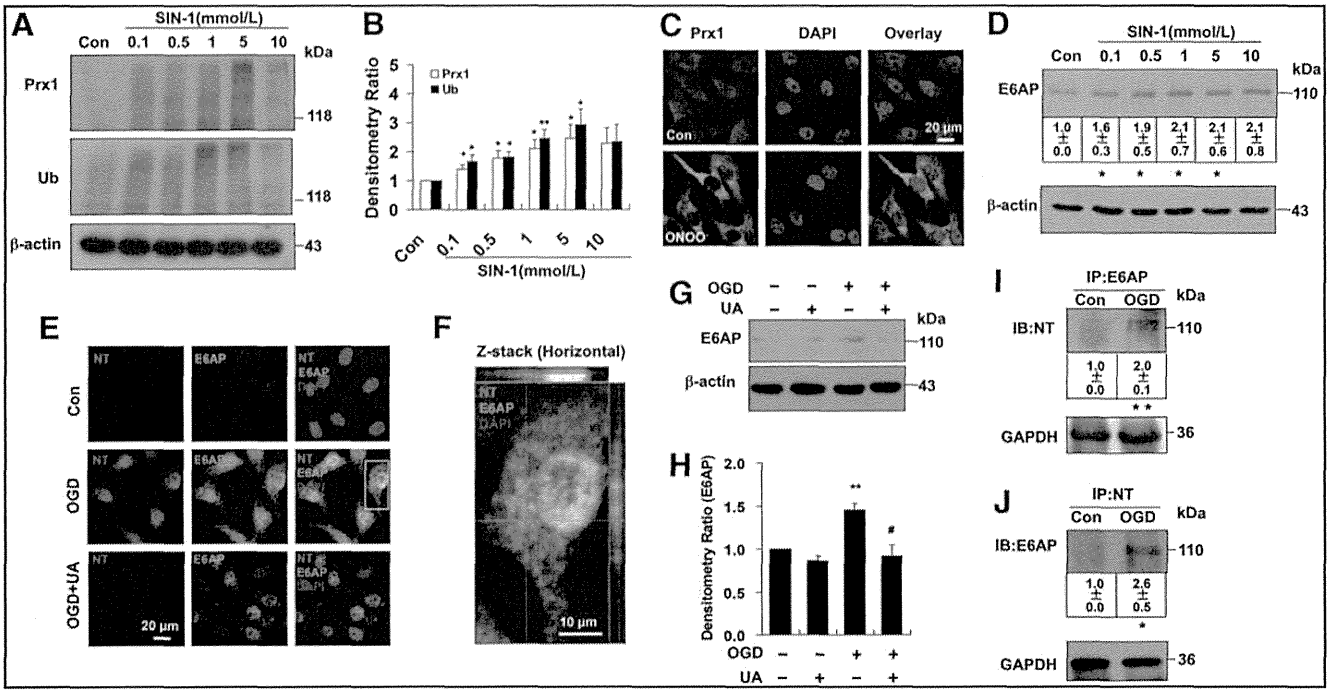

FIG. 6. Nitrosative stress is associated with ubiquitination of Prx1 in endothelial cells. **(A)** The ubiquitination of Prx1 after SIN-1 stimulation in endothelial cells. The blots were labeled with anti-Prx1 or anti-ubiquitin antibody and visualized with the ECL system. Molecular sizes are indicated on the *right*. **(B)** The SIN-1-induced changes in polyubiquitinated Prx1 were quantified and shown in the bar graph as densitometry ratio of control (mean ± SEM). $*p < 0.05$; $**p < 0.01$ *versus* control. **(C)** Immunocytochemical analysis of Prx1 level after $ONOO^-$ treatment by laser confocal microscopy. DAPI counterstaining indicates nuclear localization (blue). **(D)** The effects of SIN-1 treatment on E6AP protein levels were examined in cell lysates of endothelial cells. EA.hy926 endothelial cells were cultured with or without SIN-1 treatment for 6 h at the indicated concentrations. Immunoblots are representative of three independent experiments (mean ± SEM). $*p < 0.05$ *versus* control. **(E)** Fluorescence immunocytochemical staining of E6AP and nitrotyrosine 6 h after OGD in endothelial cells with or without 0.5 m*M* uric acid treatment. DAPI counterstaining indicates nuclear localization (blue). NT, nitrotyrosine; UA, uric acid. **(F)** Higher-magnification image of endothelial staining from the *insets* is shown in **(E)**. **(G)** Effect of uric acid on E6AP expression in endothelial cells following OGD. Immunodetection of β-actin was used as a loading control. **(H)** Quantification of E6AP protein levels was performed using densitometric analysis of the immunoblots in **(G)**. Immunoblots are representative of three independent experiments. Data are expressed as the percentage of values of control (mean ± SEM). $**p < 0.01$ *versus* control; $^{\#}p < 0.05$ *versus* OGD. **(I)** Immunoprecipitation of E6AP from cell lysates of OGD-treated endothelial cells followed by blotting with an anti-nitrotyrosine antibody. $**p < 0.01$ *versus* control. **(J)** The OGD-induced nitration of E6AP was detected by the immunoprecipitation of nitrotyrosine followed by immunoblotting with an anti-E6AP antibody. Immunoblots are representative of three independent experiments (mean ± SEM). $*p < 0.05$ *versus* control. SIN-1, 3-morpholinosydnonimine. To see this illustration in color, the reader is referred to the web version of this article at www.liebertpub.com/ars

striatum (Supplementary Figs. S9 and S10). Staining of brain sections from lentiviral-*GFP*-injected mice with a neuronal nuclear marker (NeuN) (Fig. 8B-d) and an endothelial marker CD31 (Fig. 8B-e, f) indicates that the vector successfully transduced cells in the brain. Although the lentiviral vectors might directly diffused into the brain parenchyma, the present data indicate that lentiviral vectors in cerebral ventricular can diffuse along the neurovascular scaffold. Immunohistochemical analysis of ipsilateral sections revealed stronger GFP fluorescence in tMCAO mice that formed a continuous interendothelial staining pattern that colocalized with CD31 (Fig. 8C, D).

The protective effects of Prx1 against ischemia-induced neurological and functional deficit were evaluated by the rotarod test and neurological score measurements. The neurological scores were decreased significantly, and rotarod time was increased in LV-*Prx1*-treated mice 24 h after tMCAO (Fig. 9A) and the infarct area was reduced accordingly (Fig. 9B). The breakdown products of spectrin and calcineurin were increased after tMCAO (Fig. 9C, D), coincident with BBB leakage (Fig. 9E, F). LV-*Prx1* treatment blocked the degradation of tight junction proteins zonula occludens-1 (ZO-1) and claudin5 (Fig. 9C, D, and G) and significantly reduced BBB leakage (Fig. 9E, F). LV-*Prx1* transduction reduced the $O_2^{\bullet -}$ level assessed from dihydroethidium staining in the penumbra region of mice 24 h after tMCAO (Fig. 9H, I).

Schematic illustration of the mechanisms by which nitrosative stress induces Prx1 ubiquitination during ischemic insult in endothelial cells

We hypothesize that ischemia-induced nitrosative stress causes an early increase in Prx1 production during the adaptive phase, whereas excessive or prolonged ischemia activates E6AP E3 ubiquitin ligase, which targets Prx1 for ubiquitination and degradation during the late phase, thereby degrading the Prx1-related antioxidant defense pathway and

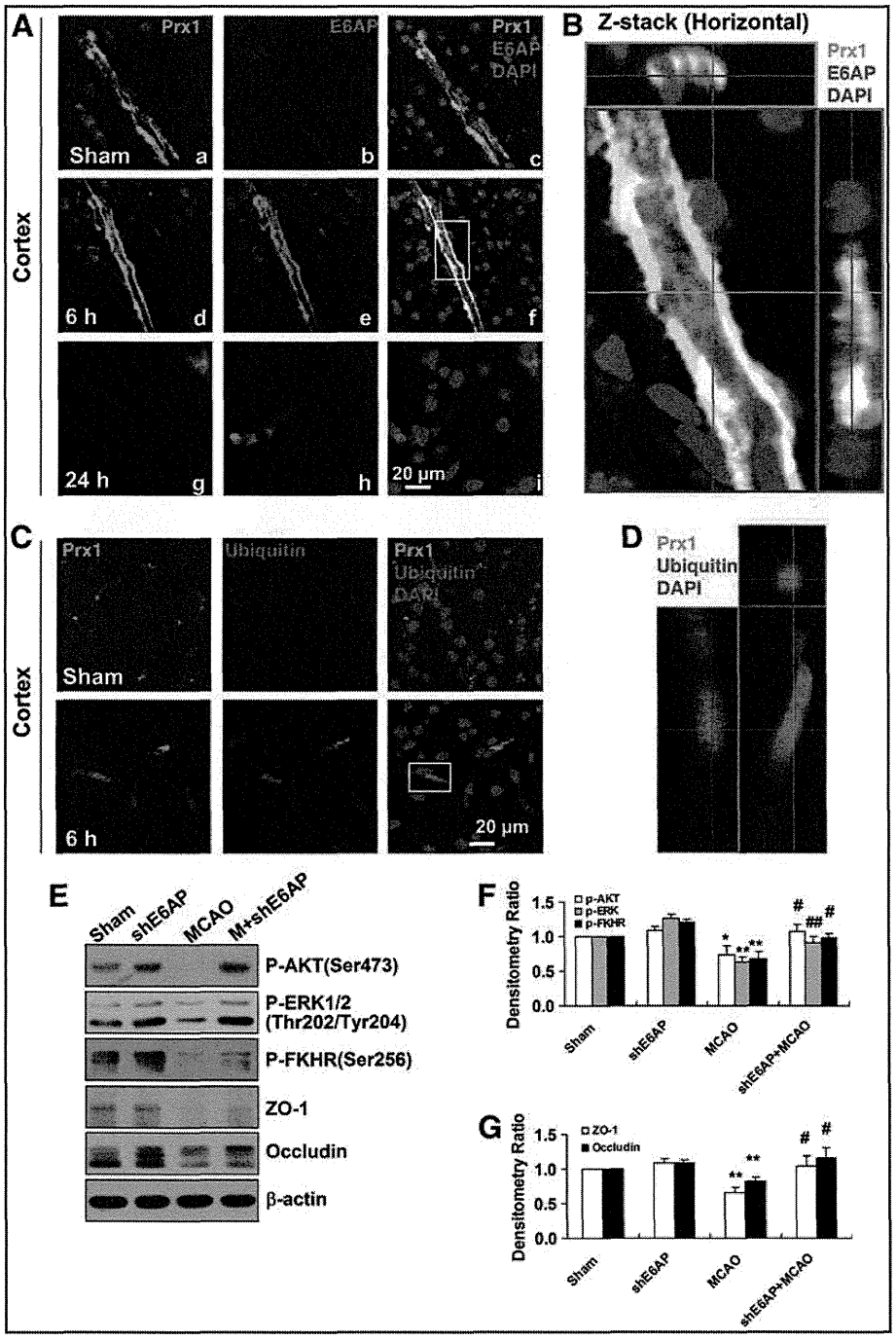

FIG. 7. E6AP activation is associated with Prx1 ubiquitination in brain microvessels of cerebral ischemia mice. **(A)** Double immunohistochemical staining for Prx1 and E6AP in the penumbra after tMCAO. Fluorescence staining for Prx1 (green) and E6AP (red) was performed in ipsilateral brain regions 6 and 24 h after brain ischemic injury in mice. **(B)** The orthogonal projections onto the $x-z$ (*upper*) and $y-z$ (*right*) planes are shown to confirm the colocalization of Prx1 and E6AP throughout the microvessels shown in **(A)**. **(C)** Fluorescence immunohistochemical staining of Prx1 and ubiquitin in brain microvessels. Anti-ubiquitin (red) and Prx1 (green) staining was performed 6 h after tMCAO in mice. **(D)** Higher-magnification image of endothelial staining from the *insets* is shown in **(C)**. Each image shown is representative of five independent mice. **(E)** The effect of *E6AP* knockdown on neurovascular damage after brain ischemia in mice. The lentivirus *E6AP* shRNA knockdown was used to silence *E6AP* mRNA. The protein extracts from penumbra brain region of mice were processed for Western blotting to detect ZO-1, Occludin, and phosphorylated AKT, ERK, FHHR. **(F, G)** Quantitative analysis of protein levels in **(E)** was performed by densitometry. Densitometry values were normalized to the average of all sham values (mean ± SEM, $n=6$). $^{*}p<0.05$; $^{**}p<0.01$ *versus* sham mice; $^{\#}p<0.05$; $^{\#\#}p<0.01$ *versus* vehicle-treated mice. Immunoblotting with an anti-β-actin antibody demonstrated equal protein loading in each lane. tMCAO, transient middle cerebral artery occlusion; ZO-1, zonula occludens-1; shRNA, short hairpin RNA. To see this illustration in color, the reader is referred to the web version of this article at www.liebertpub.com/ars

rendering the endothelial cells in the microvessels susceptible to ischemic damage (Fig. 10).

Discussion

The present study demonstrates that in endothelial cells OGD treatment leads to oxidative and nitrosative stress that engage an early increase in Prx1 production and an antioxidant response. However, more prolonged or severe ischemia-mediated nitrosative stress ubiquitinates Prx1 by the activation of E6AP ligase, thereby degrading this antioxidant defense pathway. The translational studies in mice after MCAO demonstrated that neurovascular protection was coordinated by active Prx1.

Prx1 initiates the antioxidant response by scavenging free radicals formed in response to a diverse array of cellular stresses (40, 44). Upregulation of Prx1 may be secondary to the activation of NF-E2-related factor 2 (Nrf2) (24), as *Prx1* promoter has two antioxidant response elements that are putative binding sites for Nrf2. Indeed, we recently demonstrated that Nrf2 signaling coordinates the defense against ischemia/nitrosative stress in endothelial cells (49).

The ubiquitin–proteasome system is important for protein degradation in eukaryotic cells (19, 42). Unexpectedly, ubiquitin was not highly expressed in control endothelial cells, but high-molecular-weight Prx1-polyubiquitin ladders were observed after OGD or SIN-1 treatment. The aggregation of

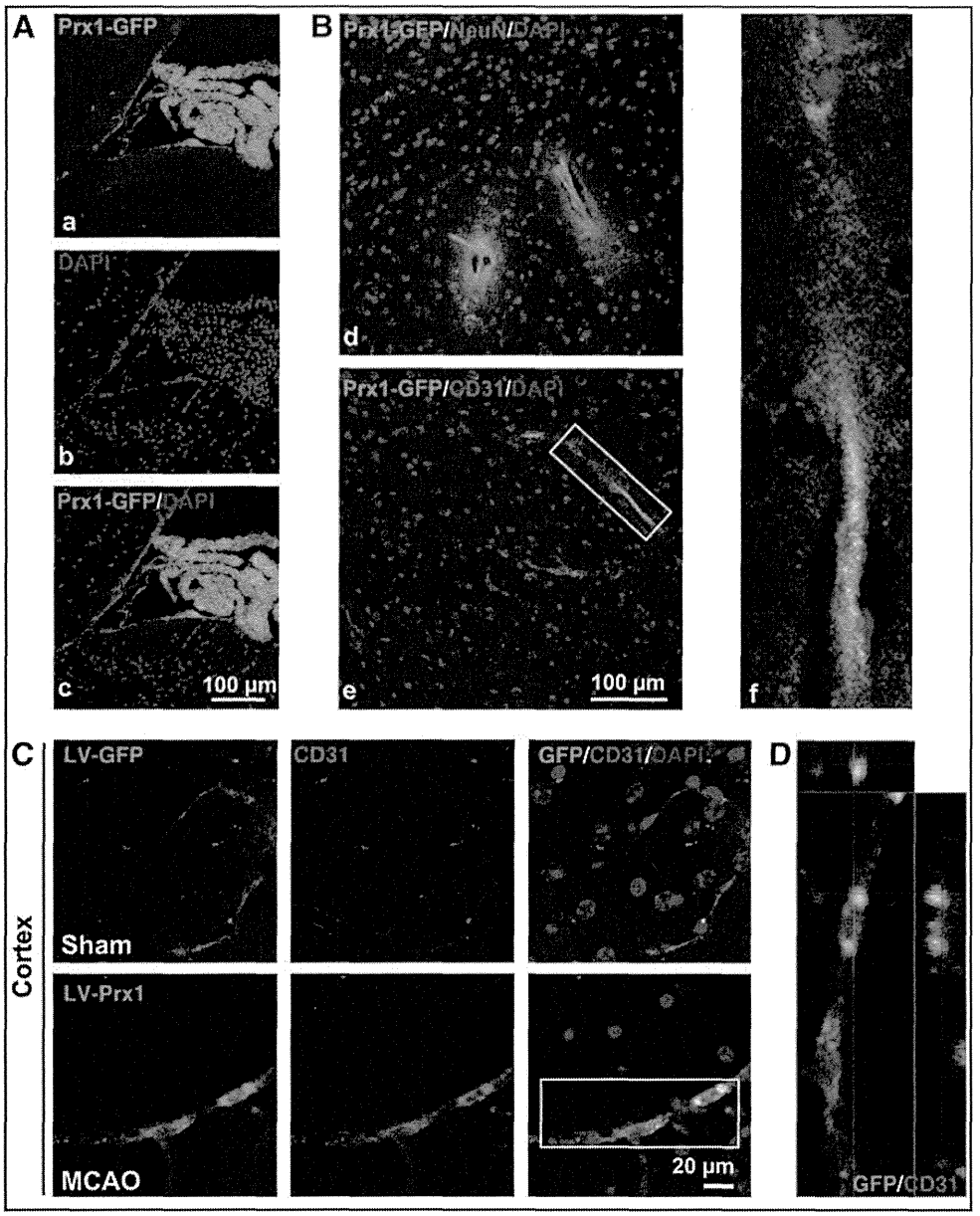

FIG. 8. The brain microvessels are the primary cell type transduced by the LV-*GFP* vector in the ipsilateral side of tMCAO mice. (**A**) The distribution of LV-GFP-Prx1 in the choroid plexus of the mouse brain 2 weeks after intracerebroventricular injection. Images demonstrate successful LV-*GFP-Prx1* transduction in choroid plexus cells. (**B**) The immunohistochemical localization of NeuN-labeled cells (red) in (**d**) and CD31-marked cells (red) in (**e**) were examined in brain cortex of mice. The *inset* (**f**) showing magnified images from (**B-e**) demonstrates the localization of GFP-Prx1 in the microvessels of the brain. (**C**) Representative immunostaining demonstrates that CD31 (red) colocalized with GFP-Prx1 on the ipsilateral side of the brain cortex 24 h after MCAO. (**D**) Representative Z-stack images shown in (**C**). Each image shown is representative of five independently injected mice. NeuN, neuronal nuclear marker. To see this illustration in color, the reader is referred to the web version of this article at www.liebertpub.com/ars

ubiquitinylated Prx1 proteins in endothelial cells after OGD reflects an imbalance between the amount of toxic unfolded proteins and the capacity of the proteasomal system to eliminate them, which may culminate in ER stress. Consistent with our *in vitro* data, there was an increased ubiquitination of Prx1 in brain microvessels of mice following MCAO that was associated with endothelial/microvessel injury. The formation of ubiquitin–protein conjugates (ubi-proteins) may mediate ischemic cell death (19, 51). A time-dependent increase in E6AP after OGD induced Prx1 ubiquitination (33). The upregulation and colocalization of E6AP with Prx1 after OGD was blunted by inhibition of nitrosative stress with uric acid or FeTPPS.

Our results identify E6AP as the E3 ligase that targets Prx1 for degradation in the later phases of OGD. Accordingly, we tested the functional relevance of this pathway in protecting the BBB of mice during tMCAO. Brain ischemia increased E6AP expression in microvessels of the penumbra region. Nitrosative stress from the reaction of NO generated by NO synthases in damaged brain cells and $O_2^{\bullet -}$ generated during ischemia underlays the ischemic cerebral cell death (17, 48). We speculate from our endothelial cell model that ischemic nitrosative stress induced the overproduction of brain microvascular E6AP. Indeed, the computational predictor evaluated 7 potential tyrosine nitration sites of E6AP with high score (Supplementary Fig. S11). Additionally, *S*-nitrosylation has been shown to modify the function of many proteins (1, 32). Therefore, it will also be important to further characterize the protein *S*-nitrosylation of thiol and amine groups during ischemia in the future.

Our finding that inhibition of nitrosative stress and redirection of E6AP restored Prx1 signaling in endothelial cells defines a new vasoprotective mechanism against the damaging consequences of ischemia. This was exemplified by the demonstration that Prx1 overexpression in the intact brain blocked tMCAO-induced neurovascular damage, attenuated

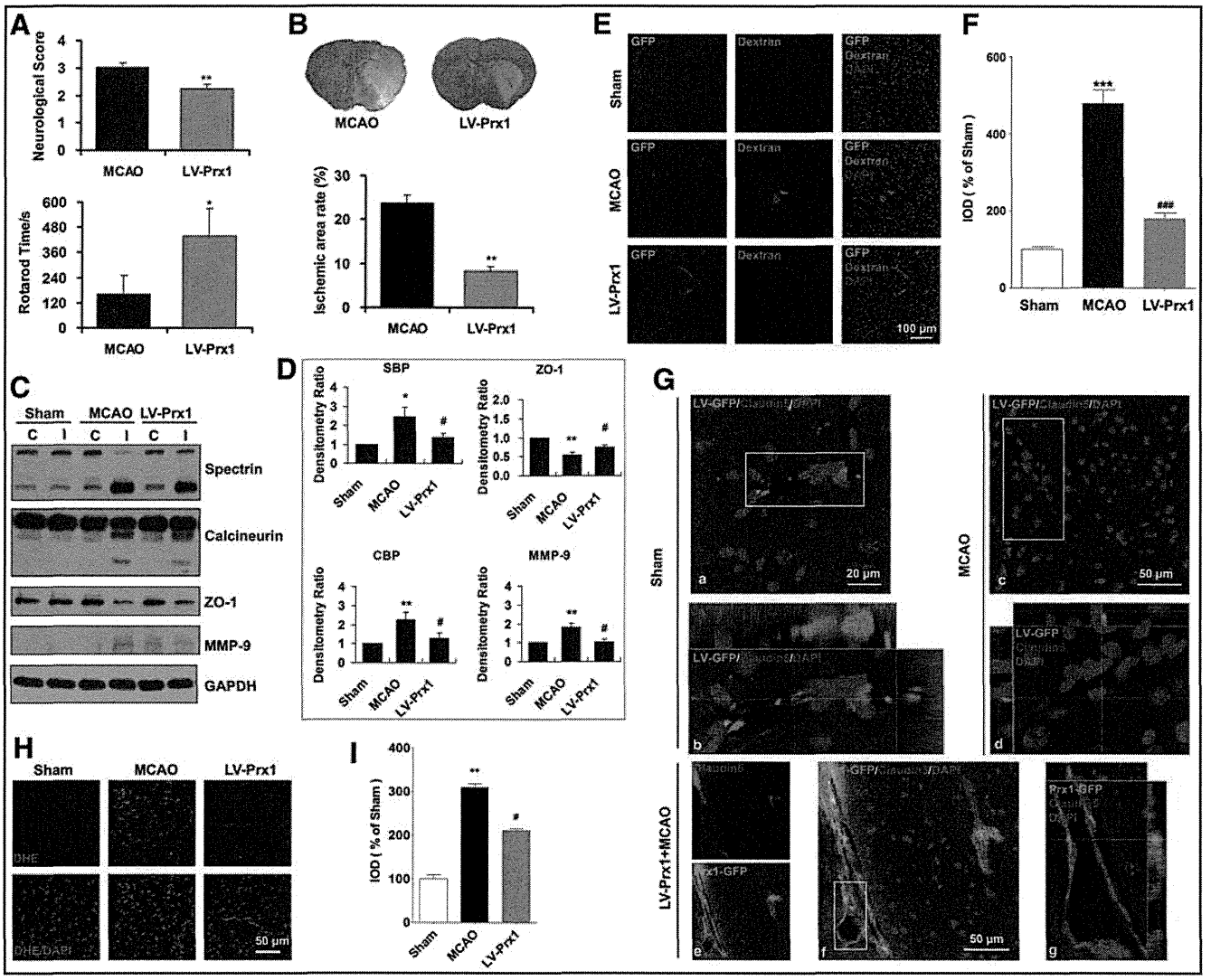

FIG. 9. Lentiviral-mediated delivery of Prx1 protects against neurovascular protection in tMCAO mice. (A) Lentiviral-mediated delivery of Prx1 improved neurological functional recovery after focal ischemia. The neurological scores (*upper*) and rotarod test (*lower*) were examined. The data are expressed as the percentage of the values observed in vehicle-treated animals (mean ± SEM, $n = 10$). $^{*}p < 0.05$; $^{**}p < 0.01$ *versus* vehicle-treated mice. **(B)** LV-*Prx1* transduction reduced the infarct area of mice 24 h after tMCAO. The mice were subjected to 45 min of MCAO, and the infarct area was quantified 24 h later in cresyl violet-stained brain sections. The data are expressed as the percentage of the infarct area/total area of each brain section (mean ± SEM, $n = 10$). $^{**}p < 0.01$ *versus* vehicle-treated mice. **(C)** The effect of LV-*Prx1* on neurovascular damage after brain ischemia. The proteins from penumbra brain region of mice were immunoblotted with antibodies against spectrin, calcineurin, ZO-1, and MMP-9, which are indicative antibodies for neurovascular damage. C, contralateral; I, ipsilateral. **(D)** The quantitative analyses are shown in the bar graph as the percentage of values of sham-operated animals (mean ± SEM, $n = 4$). $^{*}p < 0.05$; $^{**}p < 0.01$ *versus* sham mice; $^{\#}p < 0.05$ *versus* vehicle-treated mice. Immunoblotting with an anti-β-actin antibody demonstrated equal protein loading in each lane. SBP, spectrin breakdown products; CBP, calcineurin breakdown products. **(E)** LV-*Prx1* transduction attenuated BBB disruption 24 h after tMCAO. Mice were intravenously injected with Texas red-dextran in saline and perfused 120 min later. *Ex vivo* dextran labeling (red fluorescence) indicated extensive BBB permeability around disrupted brain microvessels in tMCAO mice. **(F)** Quantification of Texas red-dextran immunofluorescence expressed as integrated optical density (IOD). $^{***}p < 0.001$ *versus* sham; $^{\#\#\#}p < 0.001$ *versus* vehicle-treated mice. **(G)** Effect of LV-*Prx1* transduction on the degradation of claudin5. **(a)** Immunostaining with anti-claudin5 (red fluorescence) antibody showed brain ischemia-induced claudin5 degradation **(c, d)** in the microvessels 24 h after tMCAO. LV-*Prx1* transduction reduced the degradation of claudin5 **(e–g)** in the microvessels 24 h after tMCAO. Higher-magnification images of microvessel staining **(b, d, g)** from the *insets* of **(a, c, f)**, respectively. **(H)** The effect of *Prx1* transduction on $O_2^{\bullet -}$ levels, as determined by *in situ* dihydroethidium staining. LV-*Prx1* transduction reduced the $O_2^{\bullet -}$ level in the penumbra region compared to vehicle. Each image shown is representative of five independently injected mice. DHE, dihydroethidium. **(I)** The quantitative analyses of dihydroethidium immunofluorescence are shown in the bar graph. $^{**}p < 0.01$ *versus* sham; $^{\#}p < 0.05$ *versus* vehicle-treated mice. BBB, blood–brain barrier; $O_2^{\bullet -}$, superoxide. To see this illustration in color, the reader is referred to the web version of this article at www.liebertpub.com/ars

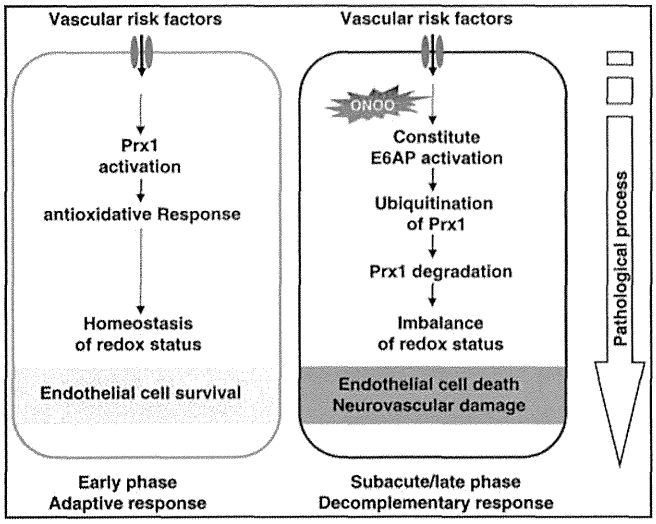

FIG. 10. Schematic illustration of the mechanisms by which nitrosative stress induces Prx1 ubiquitination in endothelial cells during ischemic insult *via* E6AP activation. To see this illustration in color, the reader is referred to the web version of this article at www.liebertpub.com/ars

BBB damage, preserved the ZO-1, and prevented the activation of metalloproteinases (MMPs). This is similar to the reports that Prx1 was required also for neurovascular cell survival during exposure to pathogenic proteins associated with brain ischemia or with amyloid-β expression in neurons (30). These results are consistent with the finding that *Prx1*-deficient mice suffer embryonic lethality because they lack essential antioxidant function (25, 34, 39). Although the neurovascular cells might be a critical issue during the earlier phase of brain ischemia, the functional coupling and collaborations among the capillaries, glia, and neurons of the brain should be taken into consideration (9, 37). For instance, recent studies highlight that pericyte loss causes BBB breakdown and neurodegeneration (2, 36). Therefore, how Prx1-mediated vascular protection contributed to the neuronal survival in the present study, however, is a topic for further investigation. Prx1 protein levels can prevent excessive ROS accumulation by interaction with thioredoxin to detoxify hydrogen peroxide (H_2O_2), $ONOO^-$, and a range of organic hydroperoxides (34). We found further that LV transduction reduced $O_2^{\bullet -}$ formation in the ipsilateral region of the ischemia brain, which might be a consequence of ERK and FKHR activation by Prx1. Indeed, Prxs participate in a very wide range of reactions, including neuronal differentiation, cell signaling, molecular chaperoning, and mitochondrial function, in both catalytic-dependent and catalytic-independent manners and can interact with JNK, c-Abl, and apoptosis signal-regulating kinase 1 (ASK1) in a redox-regulated manner (11, 14, 21, 23). Here, ipsilateral sections showed stronger GFP fluorescence in cerebral vessels of tMCAO mice, it might due to the changes of structural integrity in ischemic region, where dividing cell also largely accumulated (12, 20).

In summary, our studies identify an intracellular link between nitrosative stress and Prx1 signaling in endothelial cells following ischemia-like injury. Our description of an early ischemia-induced activation of beneficial Prx1 generation followed by subsequent inactivation represents a previously undescribed, nitrosative stress-dependent process mediated by E6AP-dependent Prx1 ubiquitination and subsequent endothelial barrier damage. Since Prx1 protected against oxidative stress in endothelial cells to reduce injury after ischemia, both *in vitro*- and *in vivo*-specific inducers of the Prx1 pathway, or mechanisms to prevent its degradation, may be targeted for therapeutic benefit in neurovascular disorders.

Materials and Methods

Reagents

Dulbecco's modified Eagle's medium (DMEM) and fetal bovine serum were purchased from Gibco. Alexa Fluor 488-conjugated anti-rabbit IgG and Alexa Fluor 594-conjugated anti-mouse IgG were obtained from Invitrogen. Uric acid was obtained from Wako. 5,10,15,20-Tetrakis-[4-sulfonatophenyl]-porphyrinato-iron[III] (FeTPPS; Calbiochem) was used as a specific $ONOO^-$ decomposition catalyst. Unless otherwise stated, all reagents and chemicals were obtained from Sigma-Aldrich.

OGD exposure and experimental treatments of cell cultures

EA.hy926 cells (16, 43), HBMECs, and mouse brain microvascular endothelial cells (bEnd.3) were used for Western blot or immunocytochemistry in the present study. Briefly, in the oxygen and glucose deprivation phase, the culture medium was replaced and washed with glucose-free Hank's balanced salt solution, after which the cultures were placed in an airtight experimental hypoxia chamber (Billups-Rothenberg) containing a gas mixture comprising 95% N_2 and 5% CO_2. To mimic an ischemia-like condition *in vitro*, cell cultures were exposed to OGD for 1, 3, 6, 12, and 24 h. Cells without OGD served as controls.

Two-dimensional gel electrophoresis

Approximately 450 μg of protein was resuspended in a rehydration solution [8 *M* Urea, 2% CHAPS, 20 m*M* DTT, 0.2% Biolyte (pH range 3–10), and 0.2% Bromphenol blue] and applied to 17-cm pH 3–10 nonlinear gradient immobiline strips for isoelectric focusing. Isoelectric focusing was performed using Protean IEF Cell (Bio-Rad), and the proteins in the IPG strips were subsequently placed on a 12% uniform sodium dodecyl sulfate (SDS)–polyacrylamide gel. The gels were silver stained and scanned with an Image Scanner in transmission mode, after which image analysis was conducted with two-dimensional PDquest (Bio-Rad). The two-dimensional gel electrophoresis was repeated three times using independently grown cultures.

In-gel digestion and mass spectrometry analysis

The in-gel digestion of proteins for mass spectrometric characterization was performed as published previously (47). After the tryptic peptide mixture was dissolved with 0.5% trifluoroacetic acid, peptide mass analysis was performed using an AB4800 MALDI-TOF/TOF mass spectrometer (Applied Biosystems). The mass spectra were externally calibrated with a peptide standard from Applied Biosystems. Based on the National Center for Biotechnology Information

(NCBI) human databases, the mass spectra were analyzed with a 50 ppm mass tolerance by GPS Explorer version 2.0.1 and Mascot version 1.9.

Plasmid constructs and transfections

The EA.hy926 or HBMEC endothelial cells were cultured in six-well plates in the growth medium and transfected with plasmid DNA encoding *Prx1*, *siPrx1*, *siE6AP*, *pRK5-HA-Ubiquitin-K48R* (17604; Addgene), or an empty plasmid control using Attractene (Qiagen). After transfection for 2 days, the cells were collected for related experiments. To express the active-site cysteine-to-alanine mutant of E6AP in endothelial cells, *p3869HA-E6AP C833A* cells (8649; Addgene) were used. The C-A mutation was introduced at the site of E6AP C833 (22, 27). The *K48R mutant ubiquitin* was obtained from Dr. Guanghui Wang (Soochow University) (27). All the constructs were confirmed by sequencing.

Lentiviral vectors preparation for brain delivery

To construct a lentiviral vector expressing Prx1, two complementary *Prx1* DNA oligonucleotides were synthesized and inserted into the *Eco*RI-*Bam*HI site of transfer vector *pCDH-CMV-MCS-EF1-copGFP* under the control of promoter *CMV*. The constructed vector was transformed into DH5a *Escherichia coli* and isolated with minipreps plasmid purification system (Promega). A large production of LV-*Prx1* was prepared by transfection of human kidney 293T cells. In brief, 293T cells were cotransfected with a mixture containing packaging plasmid (*pCD/NL-BH*DDD*), envelope plasmid (*pLTR-G*), and transfer vector and Trans-EZ. For high-titer virus stocks, the supernatant of cells was collected at 72 h after transfection, low-speed centrifuged, filtered, and ultracentrifuged. The titer of LV-*Prx1* stock was determined by transduction of HOS cells with serial dilutions of concentrated lentivirus and analyzing integrated viral DNA copies per cell by quantitative polymerase chain reaction. The lentiviral vectors coding for *GFP* without *Prx1* were prepared in a similar manner, as described above, and used as a control (LV-*GFP*). In addition, we used a lentivirus-mediated RNA interference approach to achieve the inhibition of E6AP levels in the brain. The short hairpin RNA (shRNA)-mediated *Ube3a* knockdown vectors were constructed by subcloning the U6 promoter-sh-*Ube3a* cassette into the *Age*I-*Eco*RI sites of the *pLenti-CMV* vector.

The lentiviral vector encoding mouse *Prx1* (LV-*GFP-Prx1*), LV-*GFP*, or sh-*E6AP* was injected into the right lateral ventricle over a 10-min duration using a Hamilton microsyringe with the coordinates of 0.5 mm caudal to the bregma, 1 mm lateral to the midline, and 3 mm depth from the skull surface under the guidance of a stereotaxic instrument. Two weeks after the introduction of the viral vectors, the MCAO mice model was prepared as previously reported (51). All lentivirus batches used for experiments had comparable titers ranging from 1×10^8 to 1×10^9 integration units/ml. Virus suspensions were stored at −80°C until use and were briefly centrifuged and kept on ice immediately before injection.

RNA interference

Prx1 siRNAs or *E6AP* siRNAs was introduced into EA.hy926 cells with the transfection medium according to the manufacturer's instructions. The control set of EA.hy926 cells was transfected with nontargeted siRNAs. The cells were collected for experiments 72 h after transfection. Knockdown was confirmed with Western blotting using whole cell lysates. si*Prx1* (sc-36177) and scramble negative control (sc-37007) were obtained from Santa Cruz Biotechnology: si*E6AP* (sense), 5′-GCCCAGACACAGAA AGGUUTT-3′; scramble negative control (siCont-1, sense), 5′-UUGCGGGUCUAAUCACCGATT-3′.

Annexin V/PI flow cytometry analysis

Flow cytometric assays to evaluate apoptosis by Annexin V/PI (BioVision) staining were performed essentially as previously described, following the manufacturer's instruction. Briefly, endothelial cells were transfected with *Prx1* siRNAs for 48 h before exposure to 6 h OGD. Annexin V-FITC and PI were added to the cell suspension and incubated at room temperature for 10 min in the dark. For each sample, at least 1×10^4 cells were analyzed using a FACS-Calibur flow cytometer (BD Biosciences).

TUNEL assay

In situ DNA fragmentation was assessed using a TUNEL staining combined with 4′,6-diamidino-2-phenylindole (DAPI) counterstain. Images were recorded after counterstaining with DAPI (nuclei marker), and endothelial cells were identified by phase image. Endothelial cells were imaged using 20× objectives. The apoptotic response was expressed as the percentage of TUNEL-positive endothelial cells/the total number of nuclei counted after DAPI staining. The results represented the average of a minimum of three experiments, and a minimum of 600 cells were counted per experiment.

Cell fractionation, immunoprecipitation, and immunoblotting analysis

Immunoblotting was carried out in endothelial cell lysates after determination of protein concentrations using the Bradford's solution. The cell lysates containing equivalent amounts of protein were applied to 10%–13.5% acrylamide denaturing gels (SDS-polyacrylamide gel electrophoresis [PAGE]) (15). Proteins were then transferred to an immobilon polyvinylidene difluoride membrane for 1 h at 50 V. Membranes were blocked in 20 m*M* Tris-HCl (PH 7.4), 150 m*M* NaCl, and 0.1% Tween 20 (TBS-T) containing 5% fat-free milk powder for 1 h and immunodetected with antibodies to HSP27 monoclonal antibody (1:1000), Prx1 polyclonal antibody (1:5000), (Abcam); HO-1 (1:1000), Phospho-AKT (1:1000), Phospho-ERK (1:3000), Phospho-JNK (1:1000), Phospho-P38 (1:1000), Phospho-FKHR (1:3000), and cleaved Caspase-3 (1:1000, polyclonal antibody; Cell Signaling Technology); procaspase-3 (1:2000), PARP-1 (1:2000), and ubiquitin (1:1000, polyclonal antibody; Santa Cruz Biotechnology); ZO-1 and Occludin (1:1000; Invitrogen); E6AP (1:3000) and β-actin (1:5000, monoclonal antibody; Sigma-Aldrich). After incubation for 12 h, membranes were incubated with the appropriate horseradish peroxidase-conjugated secondary antibody. Immunoreactivity was visualized by enhanced chemiluminescence (Amersham Life Science). The Prx1 ubiquitylation assays were performed essentially as described previously (46). Briefly, cells were treated with 5 μ*M* MG132 (Calbiochem)

or with dimethyl sulfoxide (DMSO; control) for 30 min before OGD. Immunoprecipitates were analyzed by immunoblotting, using either anti-ubiquitin or anti-Prx1 antibody to detect ubiquitylated Prx1. In addition, E6AP immunoprecipitates from the lysates were probed with anti-nitrotyrosine antibody.

Experimental animals

Male C57 mice, weighing 20–23 g, were obtained from the Zhejiang Medical Animal Centre (Hangzhou, China). Mice were housed under climate-controlled conditions with a 12-h light/dark cycle and provided with standard food and water. Animals were acclimated to their environment for at least 1 week before initiating the experimental protocols. All experimental protocols and animal handling procedures were performed in accordance with the National Institutes of Health (NIH) guidelines for the care and use of laboratory animals and were approved by the Committee for Animal Experiments at the Zhejiang University in China.

tMCAO model

The transient/reperfusion MCAO model was used to resemble stroke in humans (3, 5), and the surgery was carried out as previously described (18). Animal procedures were approved by the Committee on Animal Experiments at the Zhejiang University. The rectal temperature was monitored throughout the surgery, and the body temperature was maintained at 37°C ± 0.5°C with a heating pad. Neurological deficit tests were carried out at 24 h after tMCAO, including neurological scores and rotarod test. Neurological scores were determined 24 h after tMCAO using a previously described scoring system (45). Rotarod test, which started 3 days before the surgery to train five times every day, was performed to examine the motor coordination. The rotarod time (s) that mice persisted on the rotarod after ischemia was recorded; the data were expressed as the mean duration of five trials at 24 h after tMCAO. The brain infarct area of mice 24 h after ischemia was evaluated from scanned digital images of Nissl-stained brain sections using Image J software (NIH).

Evaluation of BBB damage

The loss of BBB integrity was also verified by the leakage of Texas red-conjugated dextran from microvessels after intravenous injection. Texas red-dextran (70 kDa) solution (0.1% in phosphate-buffered saline [PBS], 5 ml/kg) was intravenously administered *via* the tail vein at 22 h after the onset of MCAO. The mice were perfused transcardially with saline as above. After decapitation, brains were prepared according to the immunohistochemical methods, and Texas red-dextran leakage was determined by immunofluorescence staining (red fluorescence).

Confocal immunofluorescence staining and analysis

For immunofluorescence analysis in cultured endothelial cells, cells were fixed in 4% formaldehyde/PBS as previously reported (16). Cells were labeled with Prx1 (1:300, polyclonal antibody; Abcam), Nitrotyrosine (1:200, monoclonal antibody; Millipore), E6AP (1:300, polyclonal antibody; Invitrogen), and ubiquitin (1:200, monoclonal antibody; Cell Signaling Technology), followed by immunofluorescence using a standard protocol from PerkinElmer Life Sciences, Inc. Nuclei were stained with DAPI dihydrochloride bisbenzimide (5 μM). Immunolocalization and changes in Prx1, E6AP, and nitrotyrosine in cultured endothelial cells were visualized by confocal microscopy (Zeiss LSM 510).

For immunohistochemistry, mice were anesthetized at the time of sacrifice and transcardially perfused with 4% paraformaldehyde in PBS as previously described (16). The whole brains were immediately removed and post-fixed overnight at 4°C. Then, brains were cut into 35-μm-thick serial sections using a vibratome. Sections were incubated at room temperature in PBS with 0.01% Triton-X100 for 30 min and for 1 h in 3% bovine serum albumin (BSA) in PBS. For immunolabeling, the brain slices were incubated with antibodies targeting Prx1 (1:300; Abcam), CD31 (1:200; Santa Cruz Biotechnology), Claudin5 (1:200; Invitrogen), E6AP (1:300; Sigma-Aldrich), NeuN (1:300), and Nitrotyrosine (1:200) (Millipore) overnight at 4°C. After washing, the sections were incubated with Alexa fluor 488-conjugated anti-rabbit IgG (1:400) and Alexa fluor 594-conjugated anti-mouse IgG (1:400) (Invitrogen) in (Tris-NaCl-blocking) TNB buffer (1:400). In addition, the oxidative fluorescent indicator dihydroethidium was used to evaluate *in situ* $O_2^{\bullet -}$ generation as previously reported (45). Immunofluorescence was visualized by using a Zeiss LSM 510 confocal microscope.

Statistical analysis

The data were analyzed with *t*-tests when means between two groups were compared. For multigroup comparisons, statistical significance was determined using one-way ANOVA followed by a *post hoc* Tukey's test or Dunnett's comparison to control. All data are expressed as the mean ± SEM. A value of $p < 0.05$ was considered to be significant.

Acknowledgments

This work was supported in part by the National Natural Science Foundation of China (81120108023, 91232705, 81202533); the Zhejiang Provincial Qianjiang Talent Plan (2012R10036); the Zhejiang Provincial Natural Science Foundation of China (R2100281); NIH grants (NHLBI HL-68686, NIDDK DK-49870, and DK-36079).

Author Disclosure Statement

No competing financial interests exist.

References

1. Aracena P, Tang W, Hamilton SL, and Hidalgo C. Effects of S-glutathionylation and S-nitrosylation on calmodulin binding to triads and FKBP12 binding to type 1 calcium release channels. *Antioxid Redox Signal* 7: 870–881, 2005.
2. Armulik A, Genové G, Mäe M, Nisancioglu MH, Wallgard E, Niaudet C, He L, Norlin J, Lindblom P, Strittmatter K, Johansson BR, and Betsholtz C. Pericytes regulate the blood-brain barrier. *Nature* 468: 557–561, 2010.
3. Braeuninger S and Kleinschnitz C. Rodent models of focal cerebral ischemia: procedural pitfalls and translational problems. *Exp Transl Stroke Med* 1: 8, 2009.
4. Brunet Simioni M, De Thonel A, Hammann A, Joly AL, Bossis G, Fourmaux E, Bouchot A, Landry J, Piechaczyk M, and Garrido C. Heat shock protein 27 is involved in SUMO-2/3 modification of heat shock factor 1 and thereby